# Suppressing and Sensing with the Same Mask: Hybrid PIAA Coronagraphy and Wavefront Sensing via a Metasurface based Single Focal-Plane Optic

Thesis by
Dhwanil Patel

for

*Master's research project*

In partial fulfillment of the requirements for the
Degree of
Master of Science in Astronomy

Student ID: s3954722

Co-Supervisor: Dr. Sebastiaan Haffert

Second Corrector: Prof. Matthew Kenworthy

Project Duration: February 2025 – November 2025


Universiteit Leiden
Observatory

LEIDEN UNIVERSITY
Leiden, The Netherlands

30th November 2025

Dhwanil Patel
ORCID: 0009-0009-1899-4596

# TABLE OF CONTENTS

# ACKNOWLEDGEMENTS

My first and deepest thanks go to Sebastiaan for giving me the opportunity to work on this amazing project. It has truly been a fun and inspiring experience. I have learned so much and discovered how I want to contribute to this field. I am especially grateful to him for being so accessible, always patient, and always willing to explain even the smallest questions in great detail.

I would also like to thank everyone in the instrumentation group, especially Elena, for the suggestions, support, and helpful discussions throughout the project and also for bringing such good energy to all the group socials.

I owe tremendous gratitude to my parents Anand and Nisha, and my lovely family. Without their constant support and encouragement, I would not be where I am today. Thanks a lot for being the backbone in my life.

Finally, to my wonderful friends in Leiden and back home: thank you for tolerating my rants, listening to me ramble endlessly about my project, and simply being amazing friends. Special thanks to the "LADs" of BW 3.21a for creating a work environment where we somehow managed to get things done despite hardly working!

# ABSTRACT

Direct imaging of exoplanets requires deep suppression of starlight and accurate knowledge of the residual wavefront errors that remain after adaptive optics correction. A complex mask coronagraph can reach high contrast, but it needs very precise control of the wavefront at the focal plane. Conventional wavefront sensors sit in a different optical path. They do not measure the same aberrations that limit the coronagraph. This creates non common path aberrations. A wavefront sensor placed in the science path avoids this problem and can correct NCPA directly.

This thesis explores a metasurfaces ((MS)) that performs both coronagraphy and science path wavefront sensing in a single optic. The metasurface uses the chromatic response of subwavelength structures. In one wavelength band it provides the complex transmission needed for a complex mask coronagraph (CMC). In another band it provides the phase shift needed for a Zernike wavefront sensor (ZWFS). The ZWFS sits in the same optical path as the coronagraph. A second stage adaptive optics loop can therefore correct the true science wavefront without introducing new NCPA.

Two MS designs were studied to explore the trade between phase accuracy and transmission. One design reaches phase errors of about $\lesssim 3\%$ with transmission near $90-95\%$. The other reaches transmission above 95% with phase errors near $4-15\%$. These differences affect the coronagraphic contrast and the optimal mask diameter. End to end simulations with MagAO-X pupil were performaned to characterize the designed MS. Ideal mask sizes of $1.41\,\lambda/D$ and $1.36\,\lambda/D$ for the two designs were chosen where optimal coronagraphic performance was achieved for each.

The design with more accurate phase produces the best coronagraphic performance. It reaches a peak contrast of about $10^{-4}$. The higher transmission design reaches contrasts near $10^{-3}$. Both maintains an inner working angle near $0.7\,\lambda/D$ and a peak throughput near 70%. These results show that coronagraphic performance depends mainly on phase accuracy. Transmission errors change the optimal mask size but do not set the final contrast. Both metasurfaces also work as ZWFS. Their transmission is high, $\sim 95\%$, so the sensing behaviour is dominated by the fixed mask size. The photon noise sensitivity reaches about 1.05, compared to 1.15 for an ideal ZWFS with the size contrained by the coronagraphic performance. A non-linear reconstructor based on forward–backward propagation framework was used for reconstruction. They reconstruct phase accurately for aberrations between $10^{-4}$ rad and 1.00 rad. Closed loop tests show that the system reaches the coronagraphic floor of $\sim 10^{-4}$ in about 10 closed loop steps which correspond to $\sim 10^{-4}$ [rad] reconstruction error rms. These results demonstrate that a single metasurface can serve as a CMC and a ZWFS at the same time to improve coronagraphy and mitigate NCPAs.

# LIST OF FIGURES

# LIST OF TABLES

# Chapter 1

# INTRODUCTION

## 1.1 Context – Current state of exoplanet detection

Since the first confirmed discoveries of exoplanets in the 1990s (Wolszczan and Frail, 1992; Mayor and Queloz, 1995), exoplanet science has grown into a mature field with more than six thousand confirmed planets detected to date (from the NASA Exoplanet Archive[1]). Most of these detections come from indirect techniques such as radial velocity, transits, microlensing, and astrometry. Each method is sensitive to different regions of parameter space, leading to distinct populations in the mass–orbital-period distribution, as shown in Fig. 1.1. Radial velocity and transits dominate the overall yield because they can detect close-in, massive or large planets with relatively high signal-to-noise ratios. These methods have revealed a diverse population of exoplanetary systems that differ substantially from our Solar System.

Radial velocity and transit photometry dominate current exoplanet detections but offer limited characterization. RV yields orbital motion and a minimum mass, while transits provide radius and, in rare cases, atmospheric signatures. However, low transit probabilities and stellar noise restrict the number of quality systems accessible to these methods for atmospheric characterization (Olivier Guyon, 2018). Even other concepts such planet formation cannot be studies in detail with these methods (Lagrange, 2014). Direct imaging provides complementary information by separating the planet's light from that of the star, enabling higher-SNR spectroscopy and access to atmospheric composition, temperature, and clouds (Seager and Deming, 2010). This ability to measure a planet's own photons is crucial for detailed atmospheric characterization and for formation theories (Olivier Guyon, 2018; Lagrange, 2014; National Academies of Sciences, Medicine, et al., 2021), including the search for potential biosignatures (Madhusudhan et al., 2014). Despite the strong scientific case for expanding exoplanet discoveries through direct imaging, it remains the sparsest detection method, contributing only a small fraction ($\lesssim 1\%$) of all known exoplanets (see Fig. 1.1).

The difficulty arises from the combined challenge of extreme star–planet contrast—often exceeding $10^9$ in reflected visible light for an Earth–Sun analogue—and the fact that habitable-zone planets around Sun-like stars have orbital periods of order one year, not to mention their small angular separation of $\sim 0.1''$ at a distance of 10 parsecs. These limitations explain why nearly all directly imaged planets to date are young, self-luminous giant planets on wide orbits. Figure 1.2 compares

[1] `https://exoplanetarchive.ipac.caltech.edu`

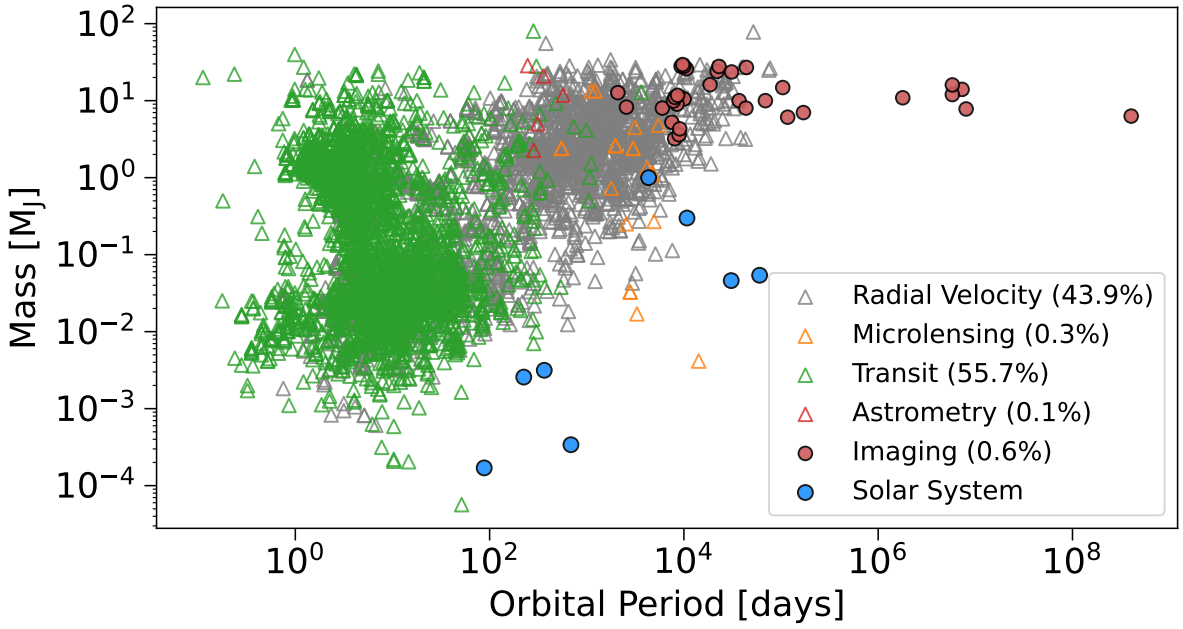


Figure 1.1: Distribution of confirmed exoplanets. The mass and orbital period of each exoplanet are shown in the scatter plot, with the color indicating the discovery technique (radial velocity, microlensing, transit, astrometry, direct imaging), together with the Solar System planets for reference. The percentage after each technique label in the legend shows the fraction of detections contributed by that method. Data retrieved from the NASA Exoplanet Archive.

the contrast required to image a self-luminous planet in the thermal infrared with that required for reflected light in the visible.

Overcoming these constraints requires high-contrast imaging systems capable of suppressing stellar light at very small inner working angles while maintaining high throughput for planetary emission.

## 1.2 Motivation

### High-contrast imaging

Directly detecting and characterizing exoplanets requires suppressing stellar light by many orders of magnitude while preserving as much planet throughput as possible. A variety of starlight-suppression techniques exist, including nulling interferometers and stellar coronagraphs. Instruments such as VLT/SPHERE (Thierry Fusco et al., 2016), Gemini/GPI (Macintosh et al., 2014), SCExAO (Jovanovic et al., 2015), and MagAO-X (Males, Close, Miller, et al., 2018) all employ coronagraphs.

Coronagraphs such as the Apodized Pupil Lyot Coronagraph (APLC) and the Phase-Induced Amplitude Apodization Complex Mask Coronagraph (PIAACMC), which are currently used on the

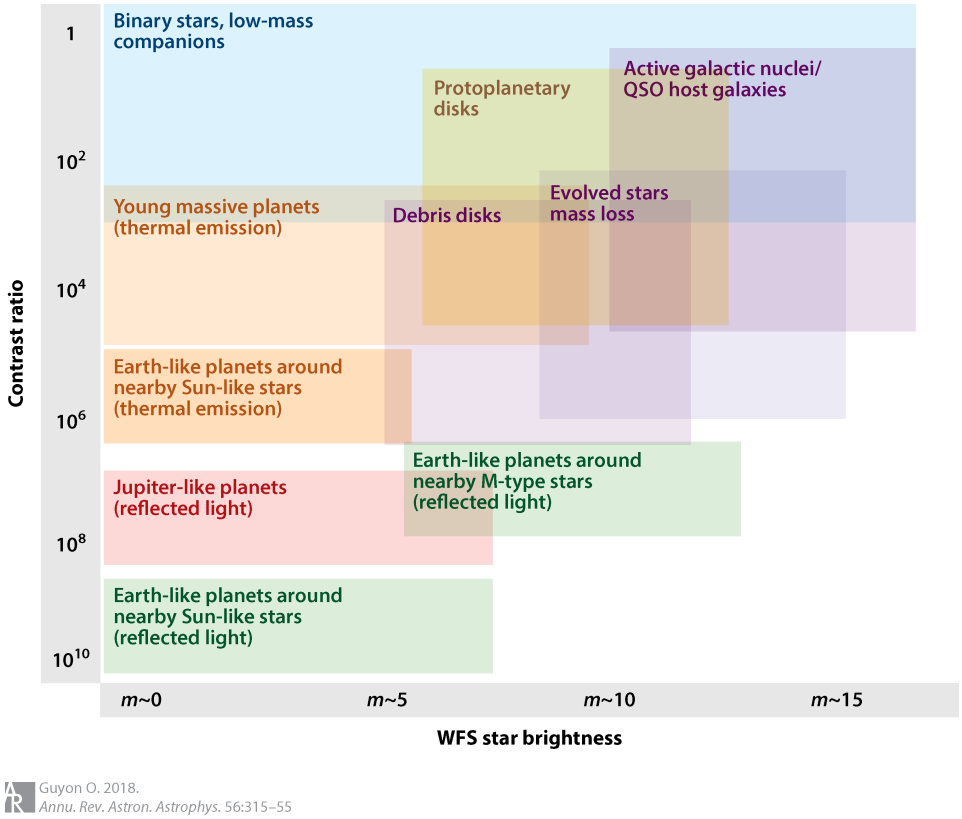


Figure 1.2: Contrast ratio required for different stellar magnitudes (adapted from (Olivier Guyon, 2018)).

aforementioned instruments, offer tighter suppression and higher throughput but require an incident flat wavefront without aberrations and therefore rely on precise sensing of wavefront aberrations (mostly from Earth's atmosphere) and wavefront control to correct for them (Kenworthy and S. Y. Haffert, 2025).

**Extreme adaptive optics and non-common-path aberrations**

Extreme adaptive optics (ExAO) systems offer the precision required to correct atmospheric turbulence at kilohertz rates to deliver high Strehl ratios (> 80% in the IR (Olivier Guyon, 2018)) necessary for coronagraphic performance. A typical ExAO system uses an on-axis guide star to measure the wavefront error using a wavefront sensor. However, the wavefront measured by the main wavefront sensor differs from the wavefront in the science channel because of optics not shared between the two paths. These non-common-path aberrations (NCPA) generate quasi-static speckles, resulting in wavefront errors on the order of a few nanometers (at visible and near-IR wavelengths) that limit contrast (N'Diaye et al., 2016).

To address NCPA, a secondary, science-path wavefront sensor is required—one with higher sen-

sitivity, as motivated in Olivier Guyon, 2005. The Zernike wavefront sensor (ZWFS), based on Zernike's phase-contrast method (Zernike, 1935), has emerged as a promising solution and has been successfully demonstrated for minimizing residual aberrations on-sky (N'Diaye et al., 2016). The PIAA–iPIAA apodization scheme needed for the CMC also improves sensitivity for the ZWFS (S. Y. Haffert, Males, and Olivier Guyon, 2023). This is due to mode matching between the input profile and the profile of the mask required for optimal interferometry (Olivier Guyon, 2003; S. Y. Haffert, Males, and Olivier Guyon, 2023), which these complex focal-plane masks naturally provide.

Because both the coronagraph and the ZWFS benefit from the same optical architecture, combining them within a single focal-plane element becomes an attractive strategy, as proposed in S. Y. Haffert, Males, and Oliver Guyon, 2023. This leads directly to the goals of this thesis.

## 1.3 Objectives – this thesis

In this thesis, we explore the use of metasurfaces to achieve simultaneous coronagraphy and wavefront sensing within a single focal-plane mask. The strong chromatic response of sub-wavelength metasurface structures enables the same optic to provide the required coronagraphic phase shift in one band and the ZWFS phase shift in another. To demonstrate this concept, we simulate a simple dual-band monochromatic phase-dot design and evaluate its performance through detailed end-to-end simulations for the MagAO-X system. We assess both the coronagraphic and wavefront-sensing capabilities of the metasurface and examine how the combined architecture behaves within a PIAA–iPIAA system.

### Thesis outlook

The remainder of this thesis is organized as follows. Chapter 2 introduces the theory and motivation behind complex focal-plane masks, covering complex-mask coronagraphy, wavefront sensing in the focal plane, amplitude apodization, and the practical considerations for combining CMC and ZWFS in a unified architecture. Chapter 3 presents the metasurface design framework, beginning with sub-wavelength structure theory, followed by meta-atom and full-device simulations used to obtain the desired complex transmission response. Chapter 4 describes the end-to-end characterization of the metasurface masks within the MagAO-X simulation environment, including coronagraphic performance, wavefront-sensing behaviour, and closed-loop control results. Finally, Chapter 5 summarizes the key results, discusses how these findings inform future metasurface mask designs, and concludes this work.

# Chapter 2

# COMPLEX FOCAL PLANE MASK

## 2.1 Complex mask coronagraphy

The classical Lyot coronagraph, introduced by Bernhard Lyot in 1939 (Lyot, 1939), employed an opaque focal plane mask (FPM) positioned at the location of the stellar PSF core, combined with a downstream pupil-plane mask known as the Lyot stop. The opaque FPM blocks the bright on-axis starlight, while the Lyot stop suppresses the diffracted light originating from the mask edges (Fig. 2.1). Although effective, this architecture has several limitations: Firstly, the residual diffraction from the pupil edges (ring of fire) remains, and further suppression of diffraction by undersizing the Lyot stop comes at the cost of reduced throughput, and secondly, any off-axis companion within the opaque mask footprint is also blocked.

To overcome these limitations, Roddier and Roddier proposed replacing the opaque spot with a transparent one in the FPM that imparts a phase shift to the core of the PSF (F. Roddier and C. Roddier, 1997). By introducing a $\pi$ phase shift over the central region of the PSF that contains about 50% of its energy. Then the modified (phase-shifted) and unmodified wavefront components destructively interfere in the downstream pupil, allowing deeper starlight suppression without a corresponding loss in throughput.

Following the formalism of Olivier Guyon et al., 2010, we generalize this concept to include a focal-plane mask with an arbitrary complex transmission. We start with assuming time-invariant fields such that,

$$E_{\text{phys}}(\mathbf{r}, t) = \Re\left\{ \mathcal{E}(\mathbf{r})\, e^{i\omega t} \right\}, \tag{2.1}$$

where $\mathcal{E}(\mathbf{r})$ represents the complex amplitude of the monochromatic field. All subsequent analysis is performed in terms of $\mathcal{E}(\mathbf{r})$.

The on-axis electric field at the entrance pupil (A-plane) is given by

$$\mathcal{E}_A(\mathbf{r}) = P_E(\mathbf{r})\, w(\mathbf{r}), \tag{2.2}$$

where $P_E(\mathbf{r})$ is the telescope pupil transmission and $w(\mathbf{r})$ is an apodization function describing the amplitude profile across the pupil.

At the focal plane (B-plane), the mask transmission is expressed as

$$M(\boldsymbol{\rho}) = 1 + (t(\rho) - 1)\, M_a(\boldsymbol{\rho}), \qquad t(\rho) = A(\rho) e^{-i\theta(\rho)}, \tag{2.3}$$

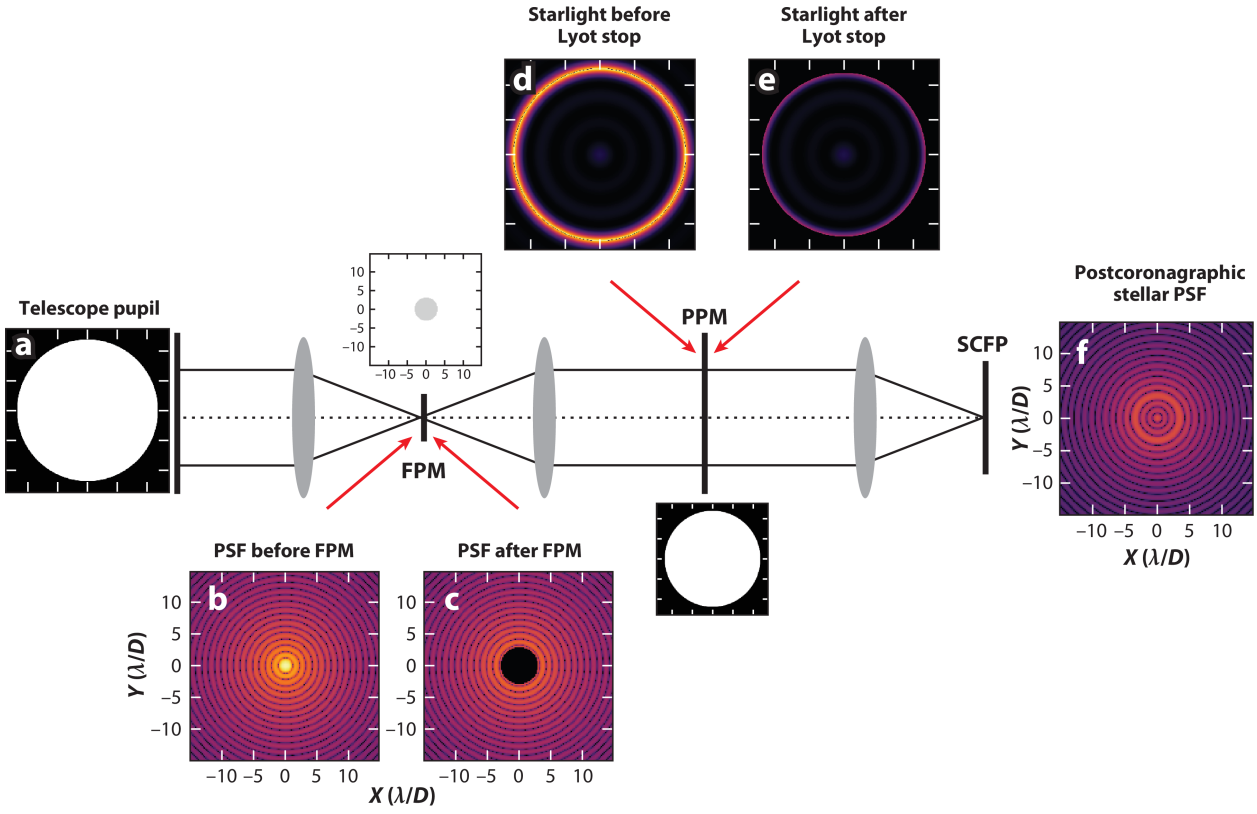


Kenworthy MA, Haffert SY. 2025
*Annu. Rev. Astron. Astrophys.* 63:179–216

Figure 2.1: Schematic of a Lyot coronagraph (adapted from Kenworthy and S. Y. Haffert, 2025). On-axis light (a) enters the telescope pupil, which is focused onto the opaque FPM that blocks the central part of the on-axis light ((b) to (c)). The residual light is then diffraction and re-imaged at the pupil-plane, resulting in a ring of fire (d) where a Lyot stop blocks this residual light (e). This is imaged onto the science focal plane (SCFP), resulting in the coronagraphic image (f).

where $M_a(\boldsymbol{\rho})$ represents a circular aperture of radius $a/2$, $A(\rho)$ is the amplitude transmission, and $\theta(\rho)$ is the phase shift introduced by the mask.

The field at the focal plane after the mask is

$$\widehat{\mathcal{E}}_B(\boldsymbol{\rho}) = M(\boldsymbol{\rho})\,\widehat{\mathcal{E}}_A(\boldsymbol{\rho}) = \Big[\,1 + (t(\rho) - 1)M_a(\boldsymbol{\rho})\,\Big]\,\widehat{\mathcal{E}}_A(\boldsymbol{\rho}), \tag{2.4}$$

where $\widehat{\mathcal{E}}_A = \mathcal{F}\{\mathcal{E}_A\}$ is the Fourier transform of the entrance-pupil field.

The field relayed to the next pupil plane (C-plane) is then obtained by an inverse Fourier transform:

$$\mathcal{E}_C(\mathbf{r}) = \mathcal{F}^{-1}\{\widehat{\mathcal{E}}_B\} = \mathcal{E}_A(\mathbf{r}) + (t-1)\,\big(\mathcal{E}_A * \widehat{M}_a\big)(\mathbf{r}), \tag{2.5}$$

where $\widehat{M}_a = \mathcal{F}^{-1}\{M_a\}$ is the inverse transform of the mask aperture function.

Inside the telescope aperture, the apodized field behaves as an eigenfunction of the operator $\widehat{M}_a$, such that

$$(P_E w_a) * \widehat{M}_a = \alpha_a \, w_a, \tag{2.6}$$

where $\alpha_a$ is the corresponding eigenvalue, which depends on both the mask size $a$ and the apodization profile (Remi Soummer, Aimé, and Falloon, 2003) and also, since within the geometric pupil $P_E = 1$, we get,

$$(\mathcal{E}_A * \widehat{M}_a)(\mathbf{r}) = \alpha_a \, w_a(\mathbf{r}) = \alpha_a \, \mathcal{E}_A(\mathbf{r}), \qquad \text{for } \mathbf{r} \in P_E. \tag{2.7}$$

Substituting Eq. (2.7) into Eq. (2.5) yields a compact expression for the relayed pupil field:

$$\mathcal{E}_C(\mathbf{r}) = \Big[ \, 1 + (t(\mathbf{r}) - 1)\alpha_a \, \Big] \mathcal{E}_A(\mathbf{r}). \tag{2.8}$$

A Lyot stop $L(\mathbf{r})$ is then applied to block diffracted light outside the geometric pupil:

$$\mathcal{E}_D(\mathbf{r}) = L(\mathbf{r}) \, \mathcal{E}_C(\mathbf{r}) = L(\mathbf{r}) \Big[ \, 1 + (t(r) - 1)\alpha_a \, \Big] \mathcal{E}_A(\mathbf{r}). \tag{2.9}$$

A complete on-axis null occurs when

$$1 + (t(r) - 1)\alpha_a = 0 \quad \Longleftrightarrow \quad t = Ae^{-i\theta} = 1 - \frac{1}{\alpha_a}. \tag{2.10}$$

In this framework, the nulling performance depends jointly on the apodization function $w_a$, which determines $\alpha_a$, and the complex transmission $t$ of the mask. Properly chosen, this combination allows perfect on-axis cancellation while maintaining high throughput for off-axis sources. This is the concept of complex mask coronagraphy (CMC).

### 2.2 Wavefront sensing using ZWFS

The same complex mask formalism can also be extended to wavefront sensing. Instead of aiming for destructive interference, the objective is to measure small phase aberrations imprinted on the incoming wavefront through intensity variations induced by the complex focal-plane mask. This concept referred as Zernike's phase contrast method (Frits Zernike, 1934) introduces a $\pm\pi/2$ to the PSF core. Similar to the Roddier and Roddier coronagraphic mask where $\pi$ shift is introduced for destructive interfernece. Such a wavefront sensor is commonly referred to as the Zernike Wavefront Sensor (ZWFS). A schematic of ZWFS is shown in the figure 2.2. Using ZWFS as means for correcting NCPA has been proposed due to it's high sensitivity (Olivier Guyon, 2005) (Bloemhof and Wallace, 2003) and it's practical implementation shown in (Mamadou N'Diaye et al., 2013) to use the intensity measurements for phase reconstruction. Here, we extend this formalism to any arbitrary complex transmission mask and also develop a linear reconstructor that works with

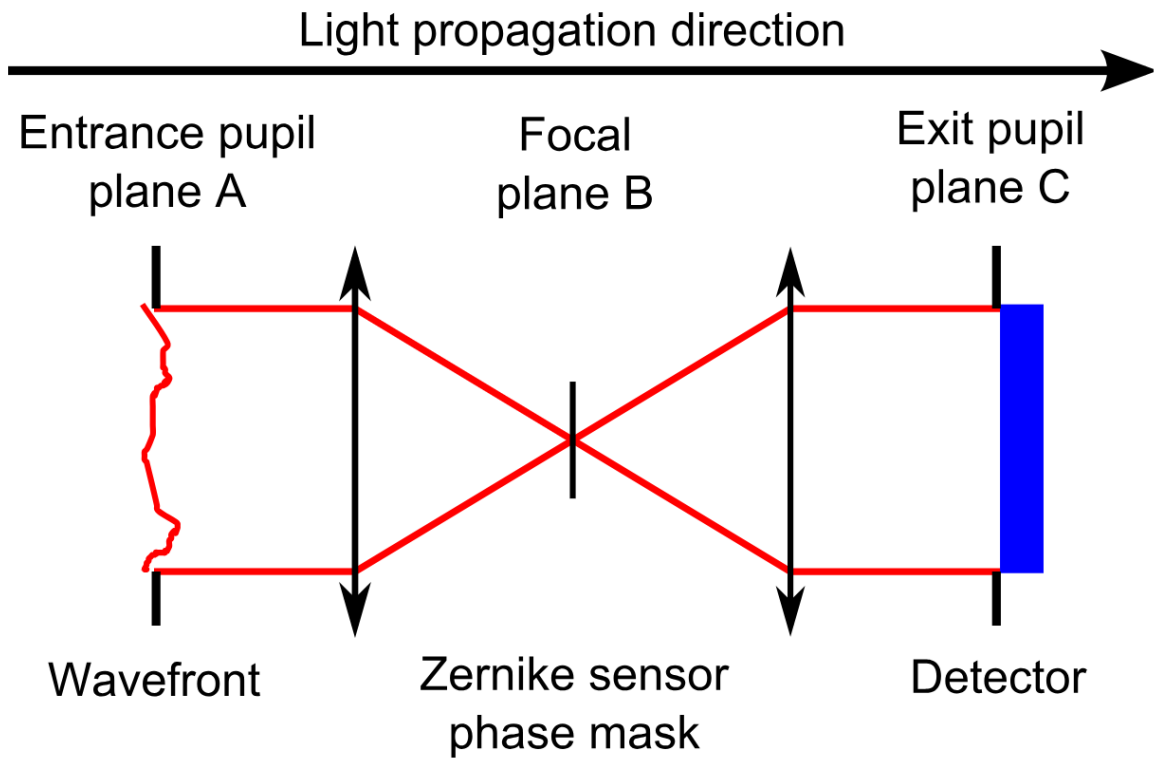


Figure 2.2: Schematic of a Zernike wavefront sensor. The aberrated wavefront (a) is focused onto the focal plane mask (FPM) (b), where the central part of the focused light passes through the mask. The masked field then interferes with the unmasked field outside the mask, and the resulting interference pattern is relayed onto the pupil plane, where the sensing camera (c) measures the intensity distribution of the interfered field. Adapted from Mamadou N'Diaye et al., 2013.

Starting again from the general propagation relation in Eq. (2.5), the entrance pupil field is allowed to include a small phase perturbation:

$$\mathcal{E}'_A(\mathbf{r}) = \mathcal{E}_A(\mathbf{r})\, e^{i\varphi(\mathbf{r})}, \tag{2.11}$$

where $\varphi(\mathbf{r})$ represents a small aberrated phase across the pupil.

Substituting Eq. (2.11) into Eq. (2.5), the relayed pupil field after the mask becomes

$$\mathcal{E}_C(\mathbf{r}) = \mathcal{E}_A(\mathbf{r})e^{i\varphi(\mathbf{r})} + \left(Ae^{i\theta} - 1\right)\left(\mathcal{E}_A * \widehat{M}_a\right)(\mathbf{r}), \tag{2.12}$$

where $A$ and $\theta$ denote the amplitude and phase transmission of the mask, respectively.

Here, $\mathcal{E}_A(\mathbf{r})e^{i\varphi(\mathbf{r})}$ is the input field $\mathcal{E}_{\text{in}}$, and $\left(Ae^{i\theta} - 1\right)(\mathcal{E}_A * \widehat{M}_a)(\mathbf{r})$ is the fixed reference field $\mathcal{E}_r$ created by the mask (for example a simple ZWFS would introduce $\pi/2$ shift). The total field relayed to the pupil plane C is therefore the coherent sum

$$\mathcal{E}_C(\mathbf{r}) = \mathcal{E}_{\text{in}}(\mathbf{r}) + \mathcal{E}_r(\mathbf{r}) = \mathcal{E}_0(\mathbf{r})\, e^{i\varphi(\mathbf{r})} + \mathcal{E}_r(\mathbf{r}), \tag{2.13}$$

where $\mathcal{E}_0(\mathbf{r}) = \mathcal{E}_A(\mathbf{r})$ is the unaberrated entrance pupil field, generally complex.

The measured intensity at the sensing pupil is

$$I(\mathbf{r}) = |\mathcal{E}_C(\mathbf{r})|^2 = \left| \mathcal{E}_0 e^{i\varphi} + \mathcal{E}_r \right|^2, \tag{2.14}$$

$$I_0(\mathbf{r}) = \left| \mathcal{E}_0 + \mathcal{E}_r \right|^2, \tag{2.15}$$

corresponding respectively to the aberrated and unaberrated cases. The differential intensity is then

$$\Delta I(\mathbf{r}) = I(\mathbf{r}) - I_0(\mathbf{r}). \tag{2.16}$$

To relate $\Delta I$ to the unknown phase $\varphi(\mathbf{r})$, the exponential term is expanded to second order:

$$e^{i\varphi} \simeq 1 + i\varphi - \tfrac{1}{2}\varphi^2. \tag{2.17}$$

Substituting into Eq. (2.14) gives

$$\begin{aligned} I(\mathbf{r}) &= \left|\mathcal{E}_0(1 + i\varphi - \tfrac{1}{2}\varphi^2) + \mathcal{E}_r\right|^2 \\ &= \left[\mathcal{E}_0(1 + i\varphi - \tfrac{1}{2}\varphi^2) + \mathcal{E}_r\right]\left[\mathcal{E}_0^*(1 - i\varphi - \tfrac{1}{2}\varphi^2) + \mathcal{E}_r^*\right] \\ &= |\mathcal{E}_0 + \mathcal{E}_r|^2 + i(\mathcal{E}_0\mathcal{E}_r^* - \mathcal{E}_0^*\mathcal{E}_r)\,\varphi - \tfrac{1}{2}(\mathcal{E}_0\mathcal{E}_r^* + \mathcal{E}_0^*\mathcal{E}_r)\,\varphi^2 + O(\varphi^3). \end{aligned} \tag{2.18}$$

Subtracting $I_0$(Eq. (2.15)) from $I$(Eq. (2.18)) and ignoring higher-order terms, yields the second-order ZWFS response:

$$\Delta I = i(\mathcal{E}_0\mathcal{E}_r^* - \mathcal{E}_0^*\mathcal{E}_r)\,\varphi - \tfrac{1}{2}(\mathcal{E}_0\mathcal{E}_r^* + \mathcal{E}_0^*\mathcal{E}_r)\,\varphi^2. \tag{2.19}$$

Recognizing the real and imaginary components,

$$\Delta I = 2\,\Im(\mathcal{E}_0\mathcal{E}_r^*)\,\varphi - \Re(\mathcal{E}_0\mathcal{E}_r^*)\,\varphi^2. \tag{2.20}$$

Solving the quadratic Eq. (2.20) for $\varphi(\mathbf{r})$ yields two possible roots; the physically relevant solution is obtained by selecting the negative sign in front of the square root, which ensures that $\varphi \to 0$ as $\Delta I \to 0$. The resulting general second-order ZWFS reconstructor is

$$\varphi = \frac{-2\,\Im\left(E_0E_r^*\right) \;+\; \sqrt{[2\,\Im(E_0E_r^*)]^2 \;+\; 4\,\Re(E_0E_r^*)\;\Delta I}}{2\,\Re(E_0E_r^*)} \tag{2.21}$$

Further approximation can linearize the Eq. (2.20), that gives the linear reconstructor,

$$\varphi(\mathbf{r}) \simeq \frac{\Delta I}{2\,\Im(\mathcal{E}_0\mathcal{E}_r^*)}. \tag{2.22}$$

Equation (2.21) thus represents the fully general second-order ZWFS reconstructor which is valid for arbitrary complex $\mathcal{E}_0$ and $\mathcal{E}_r$.

Hence, within the same formalism as the coronagraphic case, small aberrated phases $\varphi$ can be approximately reconstructed using a mask of complex transmission $t = Ae^{i\theta}$ using the linear reconstructor in Eq (2.21). For a more precise phase reconstruction, nonlinear reconstruction methods (such as the one formulated in S. Y. Haffert, 2024) can directly solve for $\varphi$ from the general intensity expression in Eq. (2.18).

### 2.3 Amplitude apodization for FPMs

Although derived separately, the complex mask coronagraph and the Zernike-type wavefront sensor share the same underlying optical architecture described by Eq. (2.5). Both rely on coherent interference between the direct and mask-diffracted fields produced by a complex focal-plane element. The difference lies only in the choice of complex transmission: in the coronagraphic regime, Eq (2.10) needs to be satisfied to produce destructive interference resulting in a nulled on-axis source, whereas in the sensing regime, we need the complex mask such that it encodes phase variations into measurable intensity. Thus, starlight suppression and wavefront sensing can be viewed as two complementary realizations of the same complex focal-plane mask theory. From Eq. (2.10), we note that the nulling condition depends on the apodization function through the eigenvalue, and it has been shown that the ZWFS's optimal sensitivity is achieved with a reference electric field that tries to mimic this top hat profile, i.e when the field is apodized (Chambouleyron, Fauvarque, Plantet, et al., 2022). Hence, for the functionalities of the FPM, apodization would push the performance towards fundamental limits. Specifically, for keeping high throughput for the coronagraph and high sensitivity for the wavefront sensor, lossless apodization is necessary.

Traditional apodization methods rely on amplitude masks placed in a pupil plane, which attenuate the outer regions of the beam to modify the pupil transmission profile. While effective, such masks are inherently lossy, reducing throughput and introducing additional diffraction from their edges. To achieve lossless apodization, Olivier Guyon, 2003 proposed the Phase-Induced Amplitude Apodization (PIAA) technique, which uses a pair of aspheric lenses (or mirrors) to remap the pupil geometrically. The first optic redistributes the incoming light so that the intensity gradually decreases toward the pupil edge, while the second optic restores the original collimation, keeping the beam collimated. This optical remapping modifies the pupil amplitude without absorbing light, thereby preserving throughput.

The required apodization is achieved by geometrically remapping the pupil illumination such that the flux enclosed within each radius remains conserved. This ensures that the total energy within the beam is preserved while reshaping the radial intensity profile to match the desired apodization

function $w_{\mathrm{PIAA}}(r)$. The aspheric surfaces of the two PIAA lenses are derived from this mapping using geometric ray-tracing and Snell's law (Olivier Guyon, 2003). The resulting pupil amplitude distribution can be directly substituted into Eq. (2.2), influencing the eigenvalue $\alpha_a$ that governs both the coronagraphic nulling condition and the ZWFS sensitivity. In this work, we use the PIAA optics designed and fabricated for the MagAO-X instrument, designed and described in detail by Foster, 2023.

### 2.4 Combining CMC and ZWFS in practice

The formalism shown in Sections 2.1 and 2.2 reveals that the complex mask coronagraph and the Zernike-type wavefront sensor are two cases of the same optical system. Both originate from the general propagation relation in Eq. (2.5) and differ only in the choice of complex transmission $t = Ae^{i\theta}$ and in the operating regime as proposed in S. Y. Haffert, Males, and Oliver Guyon, 2023. When the nulling condition in Eq. (2.10) is exactly satisfied, the on-axis stellar field is perfectly cancelled, realizing the coronagraphic mode. And when with small deviations from this regime, with the inclusion of optical aberrations, would produce residual light in the relayed pupil that encodes phase information, corresponding to the sensing mode.

The question now is how to combine both functionalities in a single focal-plane optic. The main challenge is that the coronagraphic and sensing effects occur in the same place, making their responses hard to separate. This overlap, or degeneracy, can be broken by introducing another degree of freedom, such as wavelength or polarization. For example, the mask can be optimized for coronagraphic nulling at one spectral band while another bluer spectral band can be used for wavefront sensing, as is done in a conventional adaptive optics system. Or the two functions can be separated using orthogonal polarization states within the same optical path. These approaches allow starlight suppression and wavefront sensing to operate together without needing separate focal-plane elements. Regardless, metasurfaces offer a chromatic- or polarization-specific response and hence can be employed in designing such a hybrid FPM.

In this work, we chose to exploit the metasurface for its chromatic effect and design FPMs that perform coronagraphy in the H band and wavefront sensing in the J band. For simplicity in demonstration, we consider monochromaticity for each band with a simple phase dot implementation of the complex transmission, where a $\pi$ phase dot (similar to a Roddier & Roddier mask) for coronagraphy and $\pi/2$ phase for ZWFS is considered. Since this demonstration relies solely on the phase component of the complex transmission, the mask should ideally maintain a high amplitude transmission to ensure proper implementation of the desired FPM response.

# Chapter 3

# DESIGNING THE MASKS

Building on the previous chapter, we now focus on the physical realization of the hybrid focal-plane mask using metasurfaces. Metasurfaces use arrays of subwavelength structures (or meta-atoms) to locally control the optical wavefront by engineering phase, amplitude, and polarization at each point on the surface. Unlike conventional refractive optics, where phase accumulates gradually through propagation, dielectric-metasurfaces introduce abrupt, spatially varying phase delays that can be precisely tailored by the geometry and material of each element (Yu and Capasso, 2014). This allows for an FPM capable of implementing the required wavelength-dependent phase shifts. The following sections outline the physical principles of subwavelength structures and the modelling techniques used to design and optimize their optical response. Followed by how the subwavelength structures are used to make the full FPM and analyze the optical response from the full mask.

## 3.1 Sub-wavelength structures theory

Consider a periodic array of alternating dielectric regions, for example, air ($n_{\text{air}}$) and some high-index material ($n_{\text{MS}}$) with respective widths $a$ and $b$, as shown in Fig. 3.1. When the period $\Lambda = a+b$ is much smaller than the wavelength of light, the higher diffraction orders become evanescent, and the structure behaves as a homogeneous layer characterized by an effective refractive index $n_{\text{eff}}$. This effective index depends on the geometry, constituent refractive indices, and polarization of the incident field.

This polarization-dependent behavior is rigorously described by the Rytov formalism (Rytov, 1956), which models a periodic medium as an equivalent homogeneous layer with distinct effective indices for the transverse electric (TE) and transverse magnetic (TM) polarizations. For a rectangular grating composed of materials with refractive indices $n_1$ ($n_{\text{air}}$) and $n_2$ ($n_{\text{MS}}$), and respective widths $a$ and $b$, the effective refractive indices are obtained by solving the following transcendental equations:

$$\sqrt{n_2^2 - \left(n_{\text{eff}}^{\text{TE}}\right)^2}\tan\left[\frac{\pi b}{\lambda}\sqrt{n_2^2 - \left(n_{\text{eff}}^{\text{TE}}\right)^2}\right] = -\sqrt{n_1^2 - \left(n_{\text{eff}}^{\text{TE}}\right)^2}\tan\left[\frac{\pi a}{\lambda}\sqrt{n_1^2 - \left(n_{\text{eff}}^{\text{TE}}\right)^2}\right] \tag{3.1}$$

$$\frac{\sqrt{n_2^2 - \left(n_{\text{eff}}^{\text{TM}}\right)^2}}{n_2^2}\tan\left[\frac{\pi b}{\lambda}\sqrt{n_2^2 - \left(n_{\text{eff}}^{\text{TM}}\right)^2}\right] = -\frac{\sqrt{n_1^2 - \left(n_{\text{eff}}^{\text{TM}}\right)^2}}{n_1^2}\tan\left[\frac{\pi a}{\lambda}\sqrt{n_1^2 - \left(n_{\text{eff}}^{\text{TM}}\right)^2}\right] \tag{3.2}$$

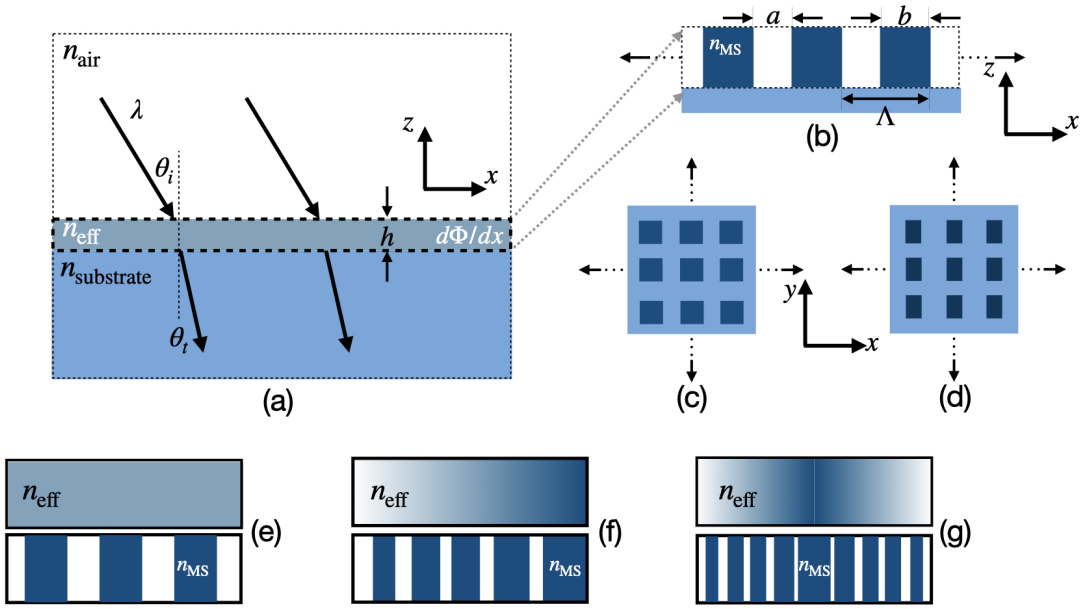


Figure 3.1: Schematic illustrating the operation and effective-medium interpretation of subwavelength metasurfaces. An incident wave at an angle $\theta_i$ interacts with a metasurface layer of height $h$ and spatially varying effective index $n_{\text{eff}}$, imparting a local phase gradient $d\Phi/dx$ that governs the refracted angle $\theta_t$ according to the generalized Snell's law (a). The metasurface is composed of a periodic arrangement of air and dielectric regions with widths $a$ and $b$ (b), forming the elementary subwavelength unit cell whose geometry determines $n_{\text{eff}}$. Arrays of such elements can be designed with isotropic (c) or anisotropic (d) cross-sections, enabling polarization-independent or polarization-selective responses, respectively. The local variation of geometry across the metasurface leads to corresponding variations in the effective index, as illustrated in (e–g), where different unit-cell dimensions result in spatially varying $n_{\text{eff}}$ that defines the desired phase and amplitude modulation.

These equations arise from enforcing the continuity of tangential electric and magnetic fields at the material interfaces. Solving them yields the effective indices $n_{\text{eff}}^{\text{TE}}$ and $n_{\text{eff}}^{\text{TM}}$, which are generally unequal, producing form birefringence that can be exploited to design polarization-selective metasurfaces. Extending this concept to two-dimensional structures, isotropic cross-sections (e.g., circular or square pillars) enforce $n_{\text{eff}}^{\text{TE}} = n_{\text{eff}}^{\text{TM}}$, resulting in polarization-independent response, whereas anisotropic geometries (e.g., rectangular or elliptical pillars) introduce polarization-dependent $n_{\text{eff}}$. Because the refractive index governs the phase and amplitude of transmitted light through the Fresnel relations, adjusting the geometry of these subwavelength elements allows precise control over the optical response.

The total phase delay imparted by a subwavelength element of height $h$ is then

$$\Phi(x) = k_0 n_{\text{eff}}(x)\, h, \tag{3.3}$$

and its lateral variation across the metasurface produces a local phase gradient,

$$\frac{d\Phi}{dx} = k_0 h \frac{dn_{\text{eff}}}{dx}. \tag{3.4}$$

On the macroscopic level, the metasurface behaves as an interface that locally modifies the phase of the transmitted wave. Applying wavevector (perpendicular to the interface) continuity across this interface leads to the generalized Snell's law,

$$n_{\text{air}} \sin\theta_i - n_{\text{substrate}} \sin\theta_t = \frac{\lambda}{2\pi} \frac{d\Phi}{dx}. \tag{3.5}$$

Thus, the microscopic modulation of $n_{\text{eff}}$ as derived from Rytov's formalism directly generates the macroscopic phase gradient that governs wavefront redirection. In this way, the metasurface represents the thin-film limit of a periodically modulated medium, where geometry-driven control of $n_{\text{eff}}$ defines the desired phase, amplitude, and polarization response.

### 3.2 Simulating subwavelength structures

We primarily focus on silicon-based metasurfaces on a silica substrate due to the architecture's familiarity. Specifically, the optical (transmission and phase) response for the meta-atoms configurations from Palatnick et al., 2024 was used as a reference to test the validity of the setup. More importantly, since we want to design our metasurface to perform in the near-infrared, we want a material with low absorption, and amorphous silicon (a-Si) exhibits that. The complex refractive index profile of the a-Si obtained from lab measurements were used for this thesis and is shown in the Fig. 3.2, and as evident, the extinction coefficient is very low for the J ($1100 - 1430$ nm) and H[1] (($1450 - 1680$ nm) bands, which are the relevant ones for this thesis.

We used the Finite-Difference Time-Domain (FDTD) method and the Fourier Modal Method (FMM) (also known as Rigorous Coupled-Wave Analysis (RCWA)) to simulate the optical response of the subwavelength unit cells (meta-atoms) and to validate the results against each other. Both techniques numerically solve Maxwell's equations, FDTD in the time domain and RCWA in the frequency domain.

The majority of the design and optimization in this work was carried out using the FDTD method due to its flexibility in handling finite-size effects and aperiodic structures, which are essential for full-device metasurface simulations discussed later in this thesis. RCWA was introduced at a later

[1]The upper wavelength limit of the H band is truncated due to the unavailability of refractive index data beyond this range.

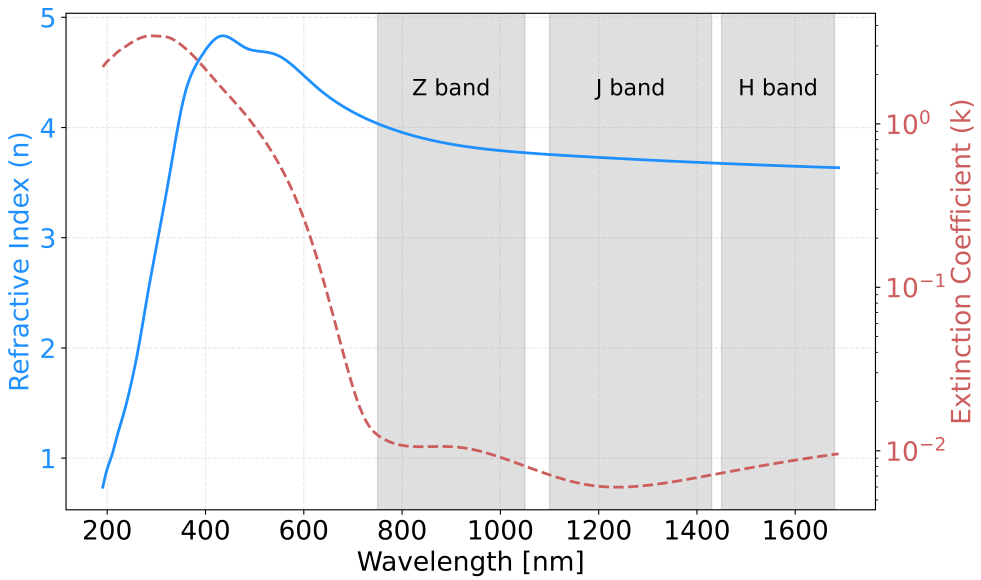


Figure 3.2: Complex refractive index profile of amorphous-Silicon. The real component of the refractive index (n) is shown in blue with the extinction in red on a log y-scale. The interested regions for thesis, Z, J and H bands are highlighted in grey. Z band was used for the validation steps described ahead.

stage primarily to validate and cross-check the single-cell optical responses obtained from FDTD. Including RCWA results provides additional confidence in the accuracy of the FDTD simulations and ensures the completeness of the modelling framework presented in this thesis.

**Fourier Modal Method**

The RCWA method is a semi-analytical frequency-domain technique that solves Maxwell's equations for periodic structures (Moharam and Gaylord, 1981). The key idea is to express both the spatially varying permittivity and the electromagnetic fields as Fourier series in the directions of periodicity. This converts the differential Maxwell equations into a matrix eigenvalue problem that can be solved layer by layer along the propagation direction.

In a typical RCWA setup, as shown in Fig. 3.3(b), the structure is modelled as layers. For example, here, the air region above the metasurface, the patterned region containing the dielectric pillar, and the substrate. Periodic boundary conditions ($BC_{\text{periodic}}$) are applied along the $x$ and $y$ directions, assuming an infinite array of identical unit cells with period $\Lambda$. Because the meta-atoms used for the final FPM are fixed to maintain a constant cross-section along the $z$-axis, the patterned layer is represented as a single uniform section. This simplification significantly reduces computational time while preserving accuracy for a normal incident source. The number of Fourier harmonics determines the precision of the solution; higher harmonics increase accuracy at the cost of computation time.

The RCWA simulations are implemented using the open-source Python package `Meent` (Kim et al., 2024). The setup involves defining the multilayer structure (superstrate, patterned layer, and substrate), the corresponding complex refractive index profiles (as illustrated in the insets of Fig. 3.3(b)), the grid resolution, and the physical height of each layer (for the meta-atom, this corresponds to its thickness along the $z$-axis). The number of Fourier harmonics in the $x$ and $y$ directions is specified to determine the level of modal decomposition, with identical values used in both directions since the metasurface is periodic with the same period $\Lambda$ along $x$ and $y$. Once these parameters are defined, the `conv_solve()` routine in `Meent` performs the complete Fourier decomposition (convolution matrix generation) and solves Maxwell's equations. The resulting scattering matrices provide the reflection and transmission coefficients for each polarization, from which the transmission amplitude and phase response of the metasurface unit cell are computed.

**Finite-Difference Time-Domain Method**

The Finite-Difference Time-Domain (FDTD) method (Yee, 1966) numerically solves Maxwell's curl equations directly in the time domain by discretizing both space and time. The computational space is divided into a three-dimensional Yee grid, where the electric and magnetic field components are staggered in space and updated iteratively over time steps using finite-difference approximations.

Figure 3.3(c) illustrates a typical FDTD simulation setup for a periodic meta-atom. Periodic boundary conditions ($BC_{\text{periodic}}$) are applied along the $x$ and $y$ directions to represent an infinite array of identical unit cells, while perfectly matched layers ($BC_{\text{PML}}$) were used along the $z$ direction to absorb outgoing waves and suppress artificial reflections. A normally incident plane-wave source is introduced below the metasurface in the substrate, propagating upward along the $z$-axis. Field monitors, $M_{\text{reflection}}$ and $M_{\text{transmission}}$, were positioned below and above the meta-atom, respectively, along the propagation ($z$) direction to record the reflected and transmitted fields.

The FDTD simulations are implemented using Lumerical's FDTD software [2] through its Python API. The global `mesh_accuracy` is set to 4, corresponding to approximately 18 grid points per wavelength, which sets the resolution of the Yee grid. The total simulation time is set to 3500 fs after some tests for the fields to reach a steady state while ensuring temporal stability. The source is defined as a normally incident plane wave of the `Bloch/periodic` type to maintain phase continuity across the periodic boundaries. It is positioned 1 effective wavelength below the substrate meta-atom interface to offset the phase accumulated during propagation through the substrate. A gap of one effective wavelength also ensures that near-field coupling with the interface is avoided. The wave is propagated upward along the $z$-axis, with its polarization angle set according to the desired polarization set. Two frequency-domain power monitors are set to record the electromagnetic fields.

[2] v.8.31.3683, Lumerical Inc.

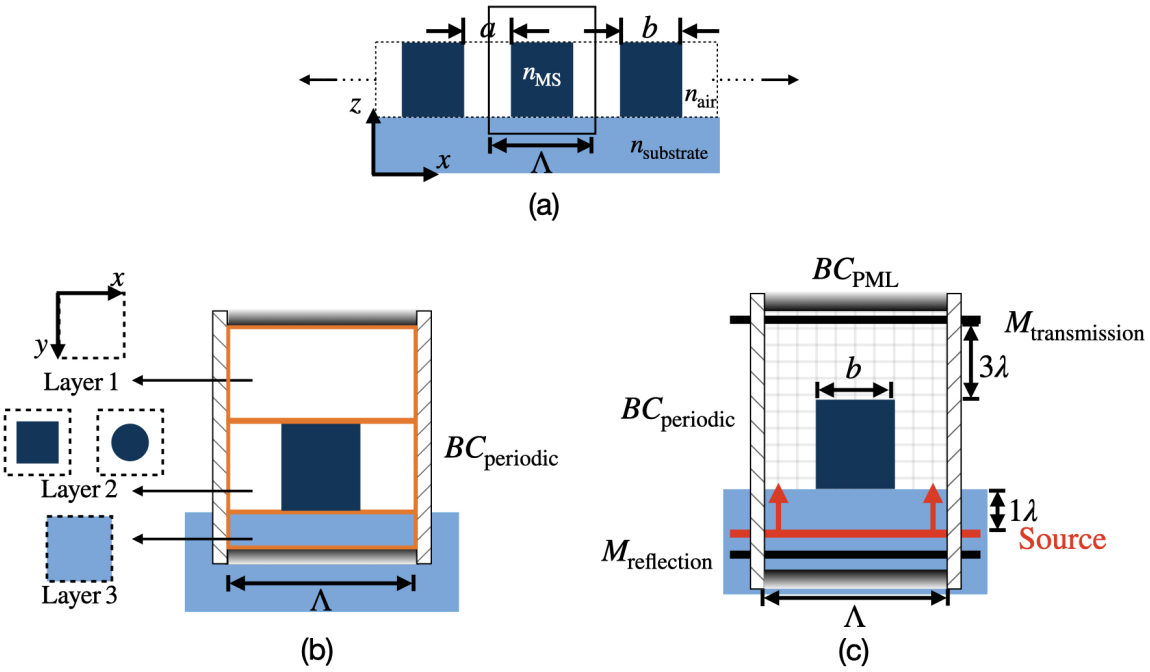


Figure 3.3: Schematic illustrating the simulation configurations used to model a single metasurface unit cell. In (a), a periodic array of dielectric and air regions with period $\Lambda$ is shown, where the meta-atom width $b$ defines the lateral dimension of the high-index region. For circular posts, $b$ corresponds to the pillar diameter, while for square pillars it represents the side length. The refractive indices of the metasurface material, air, and substrate are denoted by $n_{MS}$, $n_{air}$, and $n_{sub}$, respectively. The RCWA configuration (b) models the system as three distinct layers: the superstrate (Layer 1, air), the patterned metasurface region (Layer 2, containing the dielectric pillar), and the substrate (Layer 3, $SiO_2$), with periodic boundary conditions ($BC_{periodic}$) applied along the lateral directions to represent an infinite array. The corresponding FDTD setup (c) employs the same lateral periodic boundaries and perfectly matched layers ($BC_{PML}$) along the propagation direction. A normally incident plane-wave source, placed one free-space wavelength below the substrate, excites the structure, while the reflected and transmitted fields are recorded by monitors $M_{reflection}$ and $M_{transmission}$ positioned below and three wavelengths above the meta-atom, respectively.

$M_{reflection}$ is below the substrate, and $M_{transmission}$ is placed 3 free-space wavelengths above the top of the meta-atom. With this spacing, the measured phase comes purely from the metasurface, since any phase accumulated during free-space propagation cancels out. The monitor placement also guarantees that evanescent fields decay before reaching the monitor, so that only the propagating field components contribute to the measured transmission. The overall simulation domain extends ~1-2 free-space wavelength above and below the $M_{transmission}$ and $M_{reflection}$, respectively, to provide adequate separation between the structures and the absorbing boundaries at the top and bottom along the $z$-axis. The transmitted electric and magnetic field components ($E_x$, $E_y$, $H_x$, $H_y$) from the $M_{transmission}$ are used to compute the transmission amplitude and phase directly from the complex

field data. This approach eliminates the need for scattering-matrix post-processing.

### Validation of simulation setup

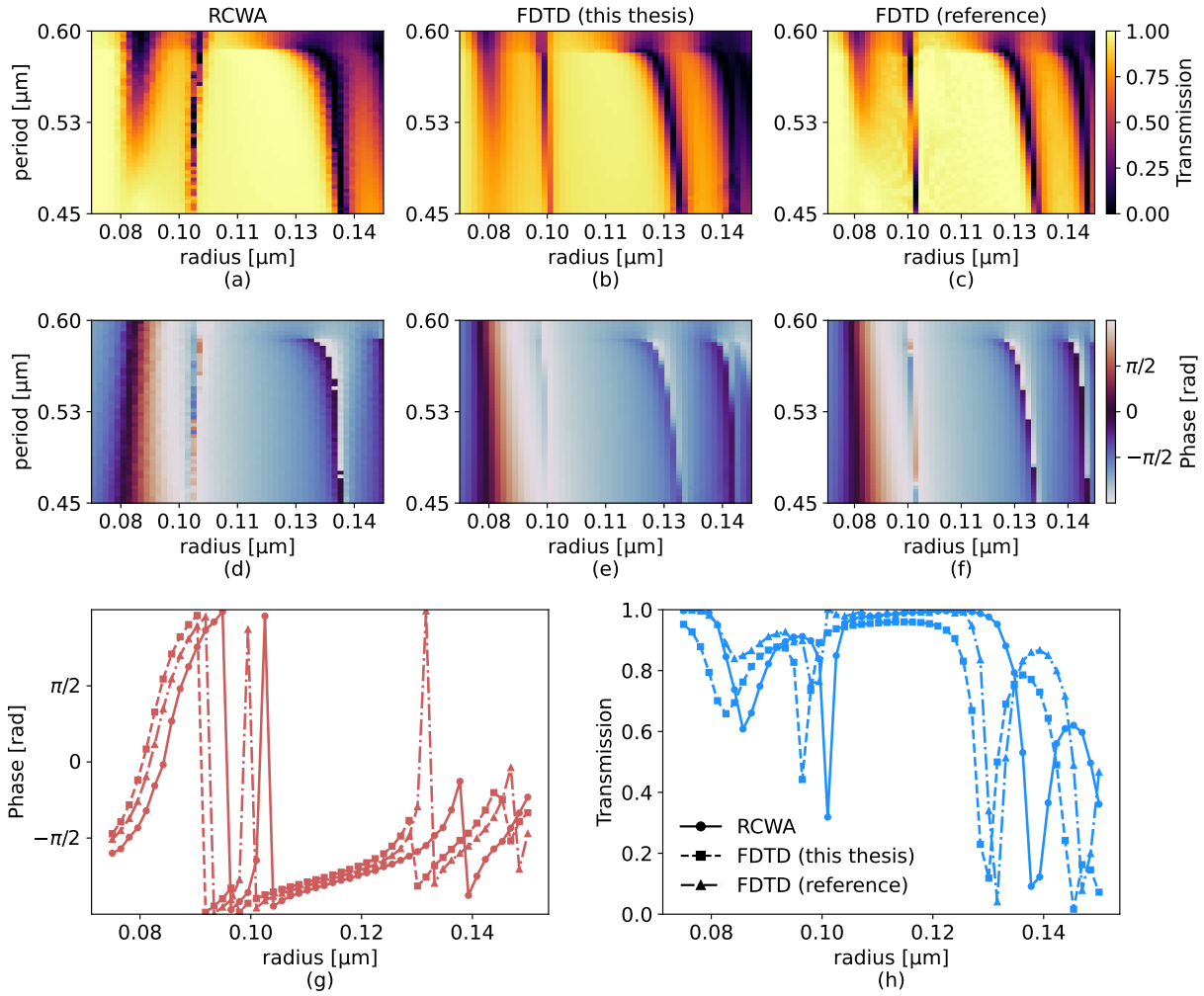


Figure 3.4: Comparison of the simulation setups with an a-Si cylindrical meta-atom on a silica substrate at 850 nm wavelength. The transmission maps as a function of pillar radius and period for the RCWA, FDTD (this thesis), and FDTD (reference) setups are shown in (a)-(c), respectively. (d)-(f) show the corresponding phase responses for the same. A line scan at $\Lambda \approx 530$ nm is plotted comparing the transmission and phase responses in (g) and (h), respectively. The three line styles represent the three methods.

Figure 3.4 compares the optical response of a representative meta-atom simulated using the FDTD and RCWA setups used in this thesis, along with the FDTD results obtained by collaborators[3] working on a similar metasurface platform as an independent reference. The simulations are carried out with a monochromatic wavelength of 850 nm for an amorphous-silicon (a-Si) cylindrical pillar

[3]First author of Palatnick et al., 2024

of height 500 nm on a silica substrate. The pillar radius ($b/2$) was varied from 75–150 nm, and the lattice period ($\Lambda$) from 450–600 nm. The 2D transmission and phase maps (Fig. 3.4(a)-(f)) show that all three simulation approaches reproduce consistent overall trends. A one-dimensional line scan at $\Lambda \sim 530$ nm (Fig.3.4(g) and (h)) provides a more direct comparison of the transmission and phase as a function of radius.

Between pillar radii of approximately 0.09-0.11$\mu$m, the apparent discontinuities in the phase arise from phase wrapping, where the phase transitions through $\pm\pi$. The wrap points occur at slightly different radii in each simulation, leading to sharp vertical jumps in the plot. This visual mismatch does not correspond to a physical phase difference, as $-\pi$ and $\pi$ represent equivalent phase states. At larger radii ($\sim 0.13\mu$m), more pronounced deviations coincide with sharp transmission minima, which correspond to resonance regions where the fields are highly sensitive to small changes in geometry or discretization. Such deviations are thus attributed to numerical sensitivity in the resonance regime and the limited number of Fourier modes used in the RCWA solver. The discrepancies between the datasets primarily come from differences in simulation parameters and numerical convergence. The RCWA simulations used a relatively low number of Fourier harmonics (3 for decomposition) and a grid size of $64 \times 64$ pixels, and the FDTD simulations employed a spatial resolution of 18 ppw (points per wavelength). Although these parameters were chosen for computational efficiency rather than precision, they are sufficient for qualitative validation of the setup. Hence, slight deviations between the results represent expected numerical artifacts rather than disagreement in the implemented methods.

Despite these regions of discrepancies, there are also stable regions such as between $\sim 0.10 - 0.12\,\mu m$ radius where the transmission is high, the both for the transmission and the phase all the three curves agrees well. Hence only for configurations with low transmission, proper convergence test needs to be done again. Having said that, for this thesis we want transmissive masks (> 85%) and hence we can go ahead with the setup. This agreement at higher transmission region validates the FDTD setup required for this thesis.

### 3.3 Meta-atom simulation results

Having established a simulation setup that we can be confident in, the meta-atom simulations for the proposed hybrid mask were carried out. An exploratory study was first performed involving parameter sweeps of different feature sizes (similar to Fig. 3.4(a) and (d)) for various geometries.

For this analysis, a wavelength of 1.57 $\mu$m and a fixed meta-atom height of 1.02 $\mu$m were used. Several geometries were examined, including cylinders, cuboids (with square bases), truncated cones, and crossed pillars. Each geometry offers distinct advantages and limitations. Structures with more degrees of freedom, such as truncated cones and crossed pillars, provide greater tunability

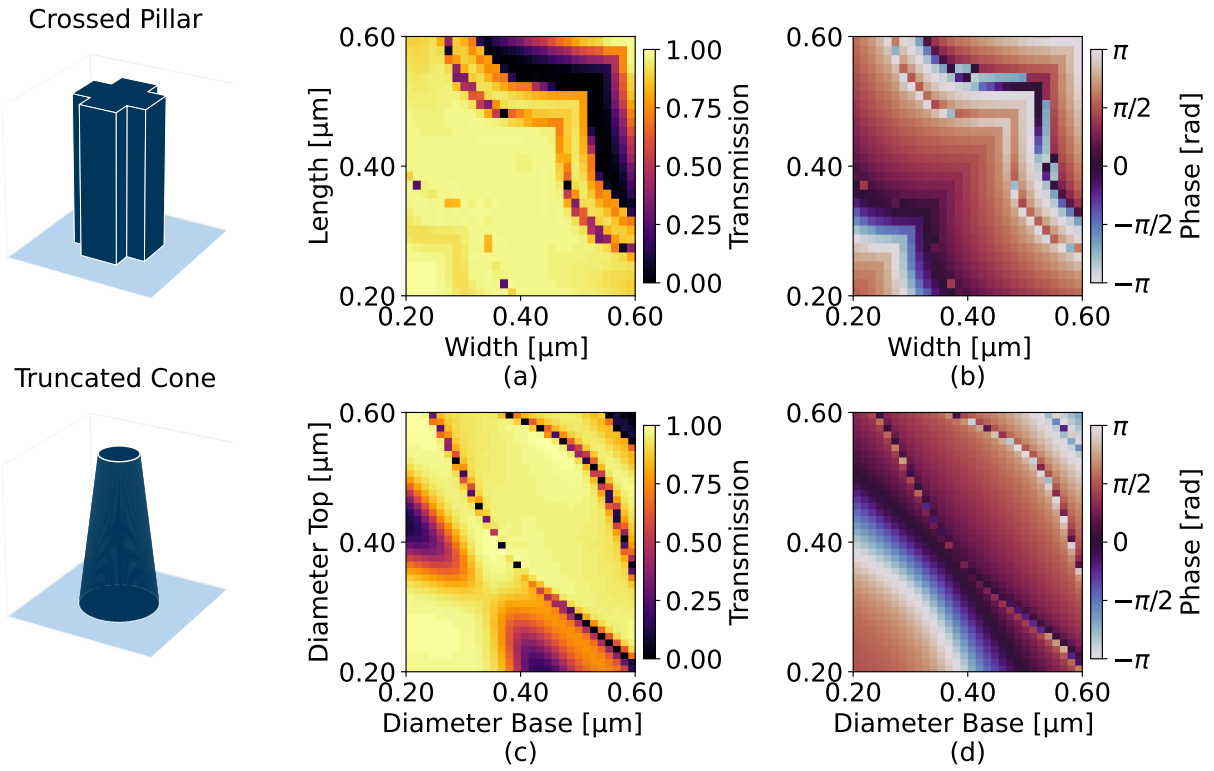


Figure 3.5: Comparison of the optical responses of different meta-atom geometries simulated with the same height ($H = 1.02\ \mu$m) and period ($\Lambda = 0.8\ \mu$m) at $1.57\,\mu$m wavelength. The top row shows the crossed-pillar geometry, where the width and length parameters (indicated by white arrows in the schematic) are varied, with the resulting transmission and phase responses shown in (a) and (b), respectively. The bottom row shows the truncated-cone geometry, with the transmission and phase responses shown in (c) and (d) as functions of the top and base diameters of the truncated cone.

in the achievable optical response but are also difficult to optimize for, not to mention they are more challenging to fabricate as well. For example, crossed pillars involve smaller feature sizes near the corners, making them susceptible to fabrication defects, while truncated cones introduce slanted sidewalls that are difficult to realize accurately.

Figure 3.5 shows the optical response for crossed-pillars and truncated cones, where the geometry of the structure itself is varied while keeping the period fixed at $0.8\,\mu$m. In the crossed-pillar case, the width and length of the rectangular pillars are varied, whereas in the truncated cone, the top and base diameters are swept. As evident from Fig. 3.5(a)–(d), there are zones of low transmission with full $-\pi$ to $+\pi$ phase coverage, and others with high transmission but limited phase coverage. The desirable region combines high transmission and complete $-\pi$ to $+\pi$ phase coverage, which in both cases lies along the diagonal where the width equals the length (for crossed pillars) or the top and base diameters are equal (for truncated cones). Along these diagonals, however, the geometries

effectively reduce to simple pillars with square or circular bases. Hence, for this application, exploring more complex geometries offers no practical advantage. Although a more refined multi-parameter scan, including variations in both period and height, could yield improved maps, such brute-force exploration at finer resolution would quickly become computationally demanding for FDTD-based simulations.

To achieve the required phase responses of $\pi$ and $\pi/2$ at specific wavelengths within the H and J bands while maintaining high transmission, we restricted the study to simpler meta-atom geometries, cylinders (with circular bases) and cuboids (with square bases), which would be sufficient for demonstrating the desired functionality. This reduction allows the exploration to focus on two key parameters: the period and the base size, as in the earlier validation study. Such geometries are also more practical for fabrication, and their symmetry ensures polarization-independent behavior.

Two complementary approaches were taken at this stage. The first was an exploratory parameter sweep of the period and base size for cuboids with a fixed height. The second used an evolutionary algorithm to optimize the period, base size, and height for cylindrical geometries.

**Searching for an ideal configuration**

The optical response of different cuboid configurations was evaluated by scanning the feature size ($S$ between 0.2–0.7 $\mu$m) and the period ($\Lambda$ between 0.7–1.0 $\mu$m) on a $50 \times 50$ grid, corresponding to step sizes of approximately $\Delta S = 0.01$ $\mu$m and $\Delta\Lambda = 0.006$ $\mu$m. The height and wavelength were fixed at $H = 1.02$ $\mu$m and $\lambda = 1.57$ $\mu$m, respectively. The choice of height was motivated by maintaining a feasible aspect ratio, with the maximum value of approximately $H/S = 1.02/0.2 \approx 5$. Figure 3.6(a) and (b) show the resulting transmission ($T$) and phase ($\Phi$) maps from this scan. These maps were then used to construct a figure-of-merit (FOM) map, shown in Fig. 3.6(c). The FOM was defined as

$$\mathrm{FOM} = T \times \exp\left(-\frac{(\Phi_{\mathrm{wrapped}} - \pi)^2}{\sigma^2}\right), \tag{3.6}$$

where $\sigma = 0.1$ rad ($\sim 5^\circ$) represents the phase tolerance. Since we aim for the highest possible transmission for these phase masks, no weighting or tolerance was applied to the transmission term. Using the defined FOM, the optimal parameters were found to be a period of 0.8026 $\mu$m and a size of 0.3292 $\mu$m, as indicated by the white arrow in Fig. 3.6(c), corresponding to FOM = 0.894 ($T = 0.89$, $\Phi = 3.135$ rad). Because sub-nanometer precision is unnecessary, the values were rounded to a period of 0.8 $\mu$m and a size of 0.329 $\mu$m, resulting in negligible changes to the response ($T = 0.893$, $\Phi = 3.134$ rad).

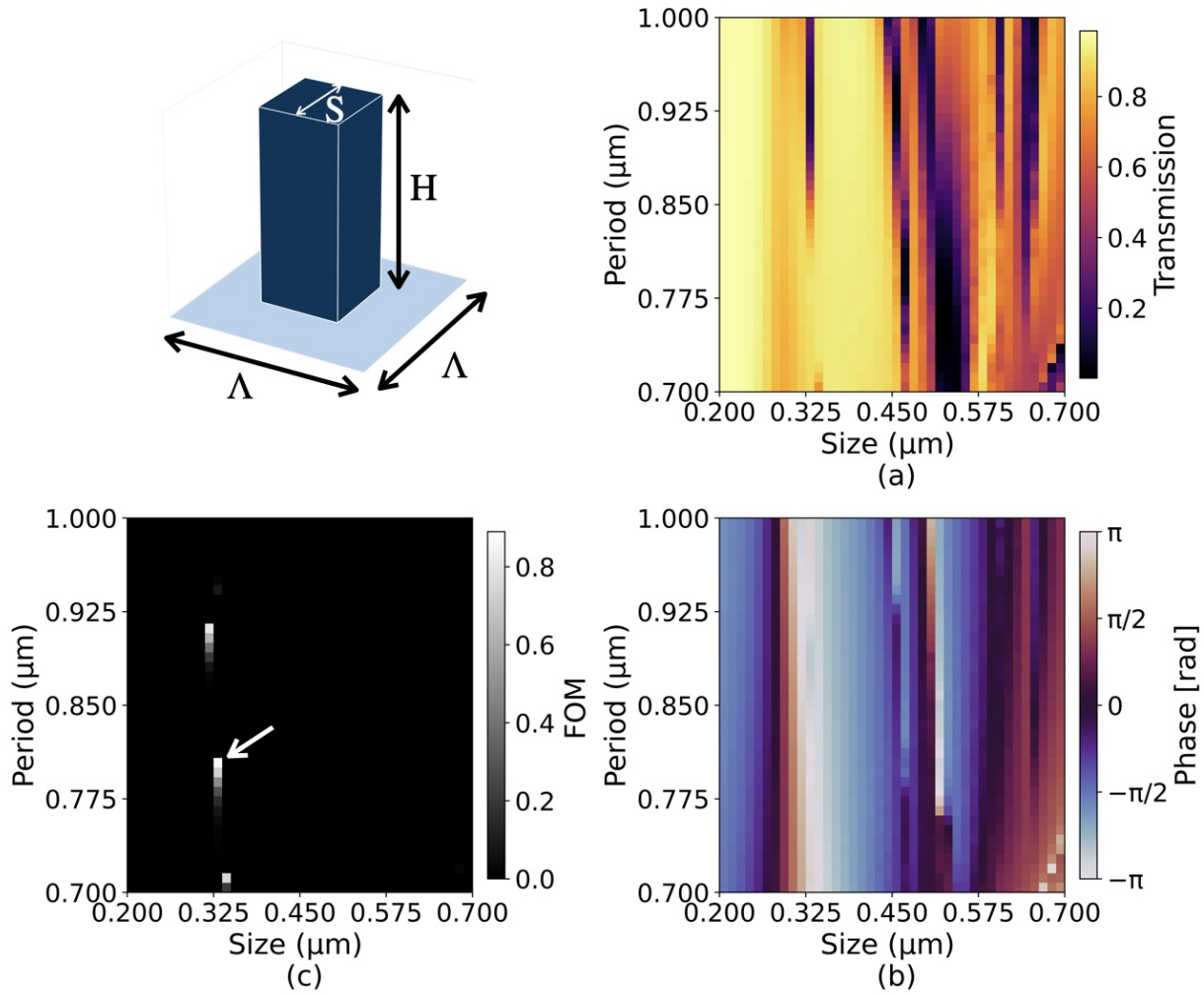


Figure 3.6: Optical response of a cuboidal meta-atom with a fixed height of $H = 1.02$ $\mu$m at a wavelength of 1.57 $\mu$m. (a) and (b) show the transmission and phase responses, respectively, as functions of the base size ($S$) and period ($\Lambda$). In (c), the figure-of-merit (FOM) map computed using the transmission and phase data based on Eq. 3.6 is shown. The optimal configuration, indicated by the white arrow, corresponds to a meta-atom providing a phase value closest to $\pi$ with the highest possible transmission.

With this, we obtained a cuboidal meta-atom configuration of height 1.02 $\mu$m, period 0.8 $\mu$m, and size 0.329 $\mu$m that provides a phase response close to $\pi$ with approximately 90% transmission at a wavelength of 1.57 $\mu$m. Using this configuration, a wavelength scan was performed within the J band to identify a region with high transmission and a phase close to $\pi/2$. Figure 3.7 shows the transmission and phase responses as functions of wavelength, with a scan step of $\Delta\lambda = 0.01$ $\mu$m. As seen from the figure, there are several regions with low transmission, but near the higher end of the J band the transmission improves, and around 1.4 $\mu$m the phase approaches $\pi/2$. Specifically, at 1.42 $\mu$m, the phase was found to be $-1.614$ rad with a transmission of 0.953. This wavelength

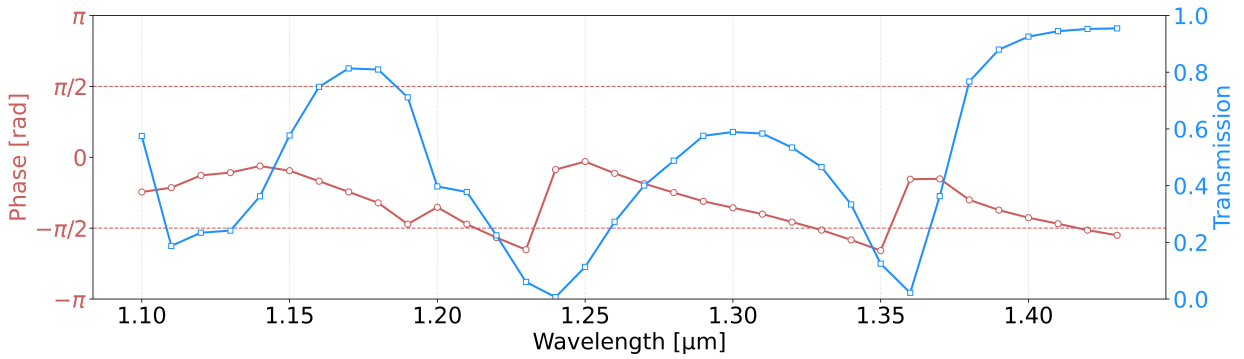


Figure 3.7: Optical response in the J band for the optimal cuboidal meta-atom. The figure shows the phase and transmission as functions of wavelength within the J band, with the red and blue curves representing phase and transmission, respectively. The red dashed lines indicate the $\pm\pi/2$ reference levels. An optimal wavelength of 1.42 $\mu$m is identified, yielding a phase of approximately 1.6 rad and a transmission of about 95%.

was therefore selected in the J band to impart a $\pi/2$ phase shift from the FPM. Hence, with this meta-atom configuration, we achieve dual functionality, imparting phase shifts of approximately $\pi/2$ and $\pi$, with corresponding transmissions of about 95% and 90%, at 1.42 $\mu$m and 1.57 $\mu$m wavelength, respectively.

It is important to note that the curve in Fig. 3.7 is not typical, and not all configurations show this type of transmission response. The transmission behaviour is mainly set by the size (or fillfactor) of the meta-atom (Yu and Capasso, 2014). A more complete optimization of the response over the full bandwidth could therefore produce a meta-atom design with a smoother and more desirable transmission profile.

**Using an evolutionary algorithm**

While scanning different geometries yielded a design that matched the phase very well, the transmission remained relatively low at $\sim$ 89% for the coronagraphic wavelength. It was therefore desirable to identify a geometry that preserved good phase performance while providing higher transmission. To explore this, we first applied an evolutionary strategy as an initial exercise. A more methodical approach was then adopted in which the wavelengths were fixed to the mean of the respective bands: 1.22 $\mu$m for the J band (wavefront sensing) and 1.63 $\mu$m for the H band. For comparison, a cylindrical meta-atom was also evaluated, with radius, height, and period treated as free parameters.

The allowed radius range was 0.0875−0.3000 $\mu$m, where the lower bound was set by fabrication constraints. The period was allowed to vary from slightly larger than the largest possible diameter (i.e., 0.75 $\mu$m) up to 1.00 $\mu$m. The height range, chosen to cover a full $2\pi$ response at the longer

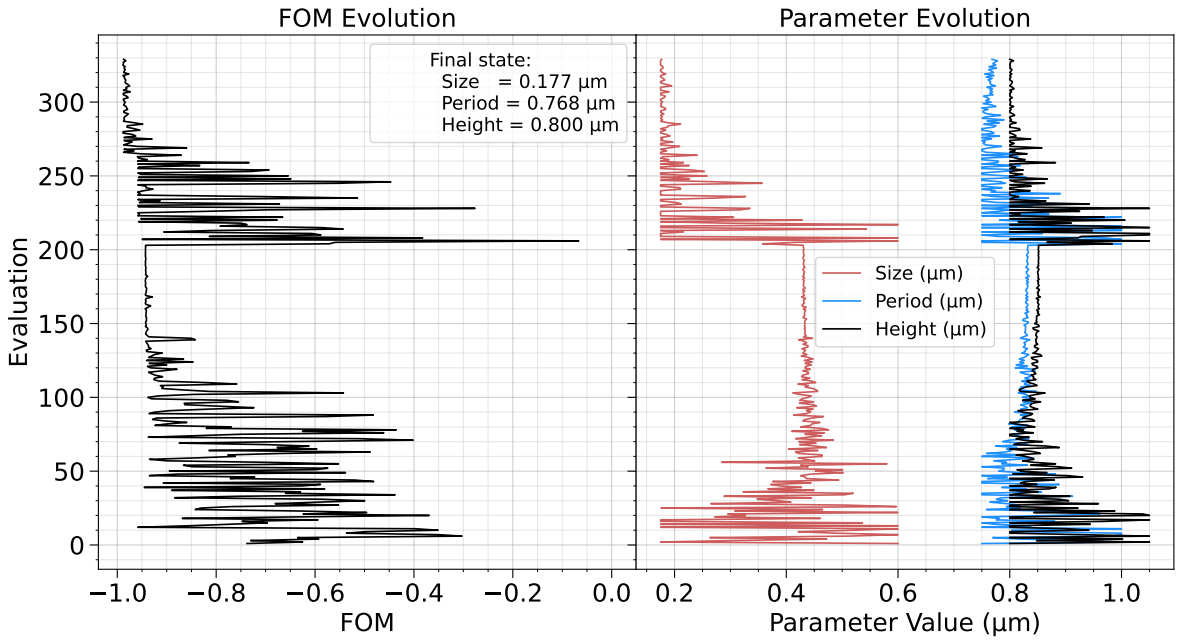


Figure 3.8: Evolution of the figure of merit (left) and free parameters (right) during the CMA-ES optimization. The final converged configuration has size 0.177 $\mu$m, period 0.768 $\mu$m, and height 0.800 $\mu$ after $\sim$ 320 evaluations.

wavelength, spanned 0.80–1.06 $\mu$m. The figure of merit (FOM) was defined as

$$\mathrm{FOM}(\Phi_J, \Phi_H, \mathrm{T}_J, \mathrm{T}_H) = 0.30\,\mathrm{T}_J + 0.30\,\mathrm{T}_H + 0.20\,e^{-d(\Phi_J, \frac{\pi}{2})^2} + 0.20\,e^{-d(\Phi_H, \pi)^2}, \tag{3.7}$$

where the weights give slightly greater preference to transmission. The angular distance $d$ is defined as

$$d(\Phi, \Phi_{\mathrm{tgt}}) = \min\left(\left|\mathrm{Arg}\left(e^{\,i(\Phi-\Phi_{\mathrm{tgt}})}\right)\right|, \left|\mathrm{Arg}\left(e^{\,i(\Phi+\Phi_{\mathrm{tgt}})}\right)\right|\right). \tag{3.8}$$

To optimize the FOM (minimizing to $-1$), the covariance-matrix–adaptation evolutionary strategy (CMA-ES) was used, implemented via the `modularCMAES` Python package (Nobel et al., 2021). The optimizer operated on normalized parameters (radius, period, height) within the range $[-1, 1]$, with a minimum step size of 0.1. Two repetitions were allowed to reduce the chance of becoming trapped in a local minima, and each repetition was allotted up to 220 evaluations unless convergence occurred earlier.

Figure 3.8 shows the evolution of the parameters and FOM. In the first repetition, the optimizer converged to a local minimum at FOM $\approx -0.9$ after roughly 200 evaluations. In the second repetition, the result improved to FOM $\approx -0.98$ within $\sim$ 120 evaluations, hence in total $\sim$ 320 evaluations were used. The corresponding optimized parameters were 0.175 $\mu$m (size), 0.770 $\mu$m (period), and 0.800 $\mu$m (height). At this configuration, the transmission in both bands exceeded $\sim$

96%, while maintaining good phase performance: approximately 15% deviation for the wavefront-sensing wavelength and $\sim$ 3% for the coronagraphic wavelength.

**Final meta-atom configurations used**

| **Meta-atom** | **Parameter [ $\mu$m]** | **Phase [** rad**]** | **Transmission** |
|---|---|---|---|
| | S = 0.329 | $\Phi_J = -1.614$ | $T_J = 0.953$ |
| Cuboid | H = 1.020 | $\Phi_H = 3.134$ | $T_H = 0.893$ |
| | $\Lambda$ = 0.800 | | |
| | S = 0.175 | $\Phi_J = -1.814$ | $T_J = 0.981$ |
| Cylinder | H = 0.800 | $\Phi_H = -3.028$ | $T_H = 0.967$ |
| | $\Lambda$ = 0.770 | | |

Table 3.1: Optimized meta-atom configurations and corresponding optical responses for two different meta-atom configurations at higher resolution of 34 ppw. The first meta-atom is a cuboid optimized for operation at 1.42 $\mu$m (J-band) and 1.57 $\mu$m (H-band), while the second is a cylinder optimized for 1.22 $\mu$m (J-band) and 1.63 $\mu$m (H-band). Each configuration consists of base size ($S$), height ($H$), and period ($\Lambda$) that results in the corresponding phase ($\Phi$) and transmission ($T$) responses at the two bands. The cuboid has transmission $\lesssim$ 95% but phase errors $\lesssim$ 3% where as cylinder has transmission $\gtrsim$ 96% but a relatively bigger phase error of $\sim$ 15% for the J band and $\sim$ 3% for H band.

## 3.4 Metasurface simulations

Having identified two suitable meta-atom configurations—a cuboid and a cylinder—that provide the desired $\pi$ and $\pi/2$ phase responses at their respective wavelengths, the next step was to simulate the full metasurfaces constructed from these unit cells. The goal here is to evaluate the overall amplitude and phase response of the complete mask at the two operational wavelengths: one in the H band and another in the J band for each configuration.

The FDTD setup used for these metasurface simulations was slightly modified from that of the meta-atom simulations. All boundaries were set to perfectly matched layers (PML) (Berenger, 1994) to absorb outgoing waves, eliminating the periodic boundary conditions used previously. This change is important because, unlike the meta-atom simulations where the structure is assumed to repeat infinitely in the lateral directions, the full-scale metasurface is finite in size. If periodic boundaries were retained, the solver would artificially replicate the metasurface, leading to non-physical interference patterns and unrealistic coupling between the edges and their periodic images. Using PML boundaries allows the simulation to capture the true physical response of a finite mask, including edge diffraction and aberrations that naturally occur where the metasurface transitions to regions without meta-atoms (Zundel and Manjavacas, 2018). These edge effects are particularly

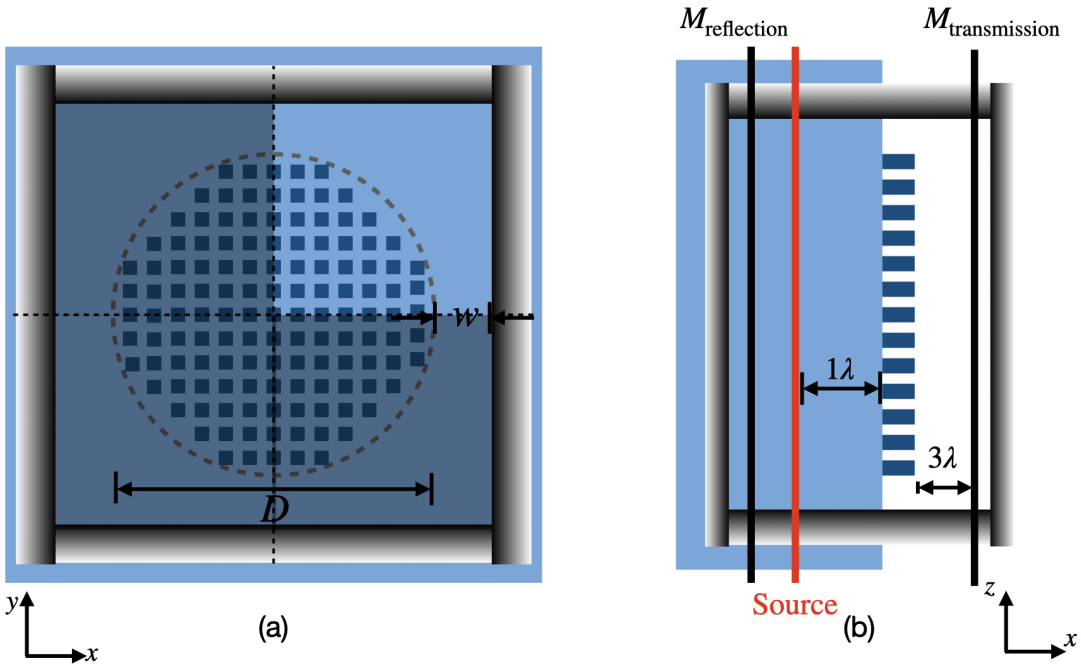


Figure 3.9: Simulation schematics of a full-scale metasurface. (a) shows the face-on ($xy$-plane) view of the metasurface of diameter $D$ (13 meta-atom periods) with a padding width $w$ between the metasurface edge and the PML boundaries. Only one quadrant is simulated because of symmetry. (b) shows the side view ($xz$-plane) of the metasurface, where the source propagates along the $z$-direction, with monitors $M_{\text{reflection}}$ and $M_{\text{transmission}}$ used to record the reflected and transmitted fields.

important to model accurately, as they can influence both the amplitude uniformity and phase stability across the transmitted field.

To save computational resources, the structural symmetry of the metasurface was exploited by simulating only one quadrant of the structure. The general layout of the simulation domain is shown in Fig. 3.9, where the metasurface of diameter $D$ rests on a silica substrate with the source propagating along the $z$-direction. Monitors were placed above and below the structure to record the transmitted and reflected fields. Owing to the symmetry of the metasurface in the $xy$-plane, simulating a single quadrant is sufficient without any loss of generality. The placement of the source and monitors was kept identical to that used in the meta-atom simulations. The simulation domain also included a padding region of width $w$ between the edge of the metasurface and the PML boundary.

Before proceeding with the full-scale simulations, the effect of the padding width ($w$) between the metasurface edge and the PML boundary was tested. The padding prevents artificial reflections and diffraction artifacts from the edges of the computational domain and provides sufficient space for the waves to decay and be absorbed properly at the PML boundary. Four different padding widths

were simulated, corresponding to 0×, 0.125×, 0.25×, and 0.375× the metasurface diameter ($D$), as shown in Fig. 3.10. These correspond to total simulation regions of 1×, 1.25×, 1.5×, and $1.75 \times D$.

The results clearly show that smaller padding widths, particularly for $w = 0$ and $0.125D$, introduce noticeable edge-related aberrations in the transmitted field. Increasing the padding reduces these effects, with $w = 0.25D$ (i.e., a total domain size of $1.5D$) providing a good balance between accuracy and computational cost. Beyond this, increasing the domain to $1.75D$ yields minimal improvement, so $w = 0.25D$ was used for all subsequent full-scale metasurface simulations.

For these padding tests, a smaller metasurface with $D = 21$ $\mu$m was used, corresponding to 28 meta-atom periods in diameter, and a spatial resolution of 14 points per wavelength (ppw). Since the purpose of this test was purely to determine the minimal padding requirement, the phase response was not analyzed in detail at this stage.

With the padding optimized, full-scale metasurfaces were simulated using 141 meta-atom periods across the diameter, corresponding to overall diameters of approximately 112 $\mu$m for the cuboid-based and 105 $\mu$m for the cylinder-based metasurface. These sizes were chosen to be as large as possible within the available computational limits of 16 GB of CPU memory (no GPU acceleration), while still minimizing finite-size effects that arise from the non-periodic boundary truncation. From rough estimates, the expected metasurface size required for its actual application would be around 200 $\mu$m, which was clearly not feasible given the current computational resources.

A reduced grid resolution of 10 ppw was therefore used to make these large-scale simulations tractable. This lower resolution introduces some phase inaccuracies, particularly for the cylindrical meta-atoms with circular bases, which generally require higher spatial resolution than those with square bases. However, the transmission results remain reliable since that depend primarily on the overall volume fill factor of the meta-atom within each unit cell.

To correct for the phase mismatch caused by the lower spatial resolution, the simulated field phase was shifted such that the mean phase from the full-scale simulation agrees[4] that of the corresponding meta-atom result obtained at higher resolution (34 ppw) to be consistent with the values listed in Table 3.1. This adjustment ensures that the overall phase reference remains consistent when the metasurface is later used as a focal-plane mask (FPM) in the hybrid coronagraph design.

Furthermore, these simulations were performed with the source illuminated through the silica substrate, meaning that light propagated from silica into air. As a result, the amplitude of the electric field must be scaled by the refractive index of silica to account for the change in medium. Following Eq. 3.9, the electric field amplitude ($|E_x|$) recorded at the FDTD transmission monitor

[4]Due to the interpolation done in the further analysis it may not exactly match the mean. But it will be within ±0.05rad.

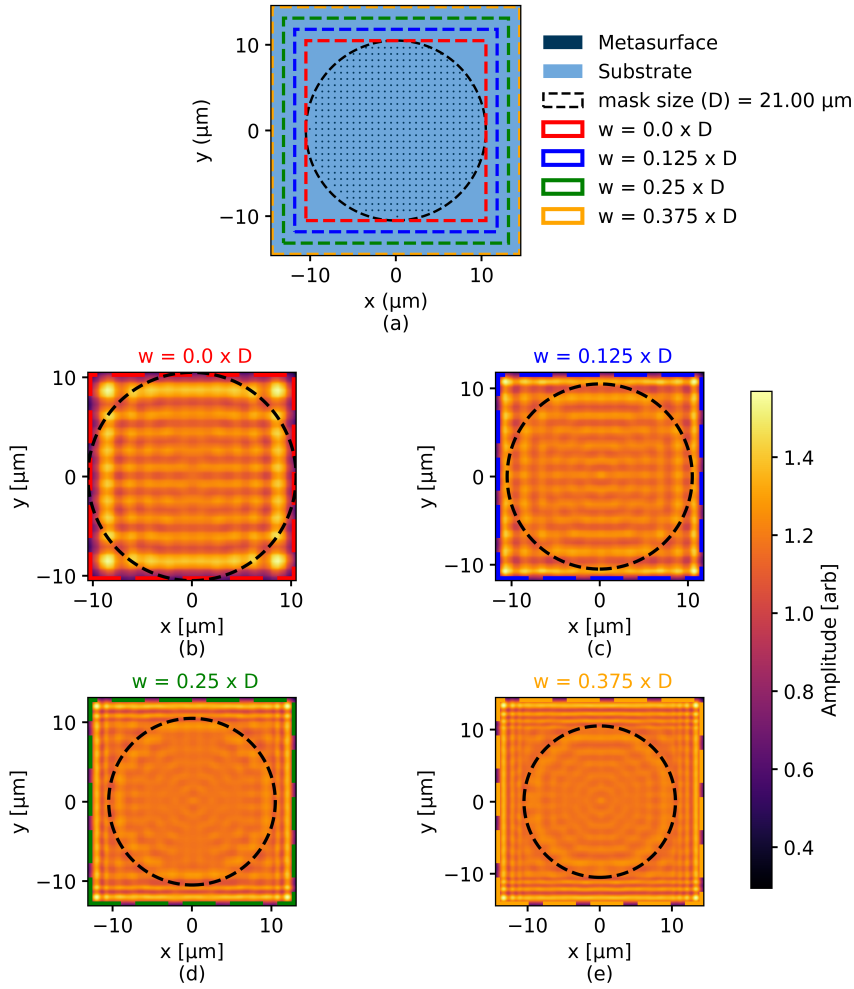


Figure 3.10: Effects of padding in full-scale metasurface simulations. Figure (a) shows the refractive index profile of a full-scale metasurface with a diameter of $D = 21$ $\mu$m, indicated by the black dashed outline. The refractive index of the meta-atoms (a-Si) is shown in dark blue, and the substrate (silica) in light blue. The red, blue, green, and orange square outlines represent the simulated regions corresponding to 1×, 1.25×, 1.5×, and 1.75× the size of the metasurface ($D$), which correspond to padding widths ($w$) of 0×, 0.125×, 0.25×, and $0.375 \times D$, respectively. Panels (b)–(e) show the amplitude of the transmitted electric field from each simulation, arranged from the smallest to the largest padding width ($w$).

was converted into the corresponding transmission map ($T$), which was then used to calculate the transmission amplitude ($E'_x$) applied in the FPM. It is worth noting that some pixels in the $T$ map exhibited transmission values slightly greater than unity. These are numerical artifacts that manifest as artificially amplified transmission points. While such features might initially appear to resemble a physical metasurface response, genuine amplification of this kind typically arises from diffraction coupling in complex metasurfaces composed of multiple, non-identical meta-atoms—where the effect extends across several unit cells (Palatnick et al., 2024). In contrast, the single-cell periodic

designs used here do not support such effects. Therefore, for our purposes, these anomalous pixels were clipped and the transmission map was normalized such that its maximum value was unity.

$$E'_x = \sqrt{T} = \sqrt{|E_x|^2 \times \left(\frac{1}{n_{\text{substrate}}}\right)}. \tag{3.9}$$

This correction is important because, in the optical simulations, the FPM is applied as an apodizer to the incoming wavefront—modifying both its phase and amplitude—where the incident light originates from air. Alternatively, the refractive index mismatch could be incorporated by using the effective wavelength within the substrate for the apodizer function; however, the scaling approach used here achieves the same result and aligns more directly with the FDTD output.

Finally, some post-processing was necessary to match the pixel resolution. The transmission amplitude and phase maps obtained from the FDTD simulations correspond to a finite-size mask with a fixed number of pixels. To ensure consistency with the focal-plane sampling used in the optical simulations, the field maps were interpolated to match the number of pixels in the simulation grid and cropped to the desired FPM diameter.

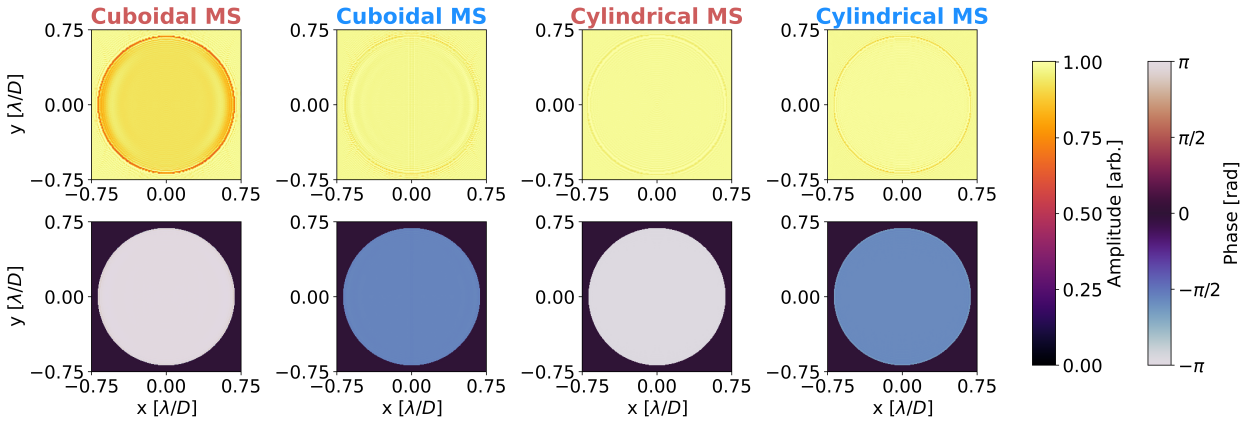


Figure 3.11: Final transmission amplitude and phase of the metasurfaces (MS) used for the a FPM of diameter 1.5 $\lambda$/D. Transmission amplitude and phase maps processed from the field monitors from the FDTD simulation of the cuboidal and cylinderical metasurface (MS) for the respective J and H band wavelength (titled blue and red color).

The final transmission amplitude and phase (i.e., complex transmission) maps for all four cases—two metasurfaces across two wavelength bands—are shown in Fig. 3.11. As seen in the figure, the complex transmission maps are largely free of numerical artifacts, suggesting that the simulation setup was well converged. The remaining visible features are likely physical in nature.

All four amplitude maps show slight irregularities near the mask boundaries, which primarily arise because, at the edges of a finite metasurface, the periodic assumption no longer holds.

Here, the structure transitions abruptly from a populated array of meta-atoms to an unpatterned region, resulting in localized amplitude distortions (Yu and Capasso, 2014). This effect is more pronounced for the cuboidal metasurface at 1.57 $\mu$m, where the transmission is comparatively lower (see Table 3.1). In principle, such effects can be mitigated by selecting meta-atom configurations that maintain very high transmission ($\gtrsim$ 92%) at the operating wavelength which is evident from the other transmission amplitude plots of other 3 cases. Some additional high-frequency oscillations are also noticeable in certain regions of the maps. These are likely caused by resonance effects inherent to subwavelength dielectric structures (Yu and Capasso, 2014) whose effects must be studied since they cannot be mitigated for.

# Chapter 4

# CHARACTERIZING THE MASKS

Having obtained the complex optical response from the metasurface simulations, we now use these results as functional focal-plane masks (FPMs) in an end-to-end optical simulation of the system. This chapter focuses on characterizing the performance of these hybrid masks—specifically, how the metasurface-based FPMs perform in their intended coronagraphic and wavefront-sensing modes.

The simulated complex transmission of each metasurface, containing both phase and amplitude information, is used directly as the mask function in the optical model. This enables a realistic assessment of the system-level performance without assuming idealized, phase-only mask behavior. In the coronagraphic mode, key performance metrics such as throughput and contrast are evaluated, while in the wavefront-sensing mode, the dynamic range and sensitivity are analyzed. And they are then use simulataneuosly in closed-loop configuration to assess them simulataneously.

The following sections describe the optical simulation setup, the methodology used for performance characterization, and the resulting metrics that illustrate how the metasurface FPMs perform relative to their ideal counterparts.

## 4.1 Setting up the MagAO-X in simulation

### MagAO-X parameters

For the characterization of the focal-plane mask (FPM) within a realistic optical system, we model the MagAO-X instrument. MagAO-X is an extreme adaptive optics (AO) system installed on the 6.5 m Magellan Clay Telescope, designed for high-contrast imaging and coronagraphy (Males, Close, S. Y. Haffert, et al., 2024). The optical beam size for the instrument is 8.9 mm. The motivation for using the MagAO-X pupil lies in the availability of a well-characterized PIAA (Phase-Induced Amplitude Apodization) lens pair, which provides a realistic apodization profile for the incoming wavefront. These lenses are fabricated from calcium fluoride ($CaF_2$), and their detailed design and fabrication process are described in Foster, 2023. The radial profiles of the PIAA lenses are shown in Fig. 4.1(c). The two lenses are separated by 60.2 mm, and an identical pair of lenses in reversed order is used downstream as the inverse-PIAA system to restore the pupil to its original geometry. For the coronagraphic channel, a Lyot stop is placed before the inverse-PIAA lenses to block the diffracted starlight originating from the focal-plane mask. This step is critical, as without it, the inverse-PIAA would reshape and re-image the diffracted light, degrading the achieved contrast. A dedicated Lyot stop matched to the PIAA-modified pupil geometry was

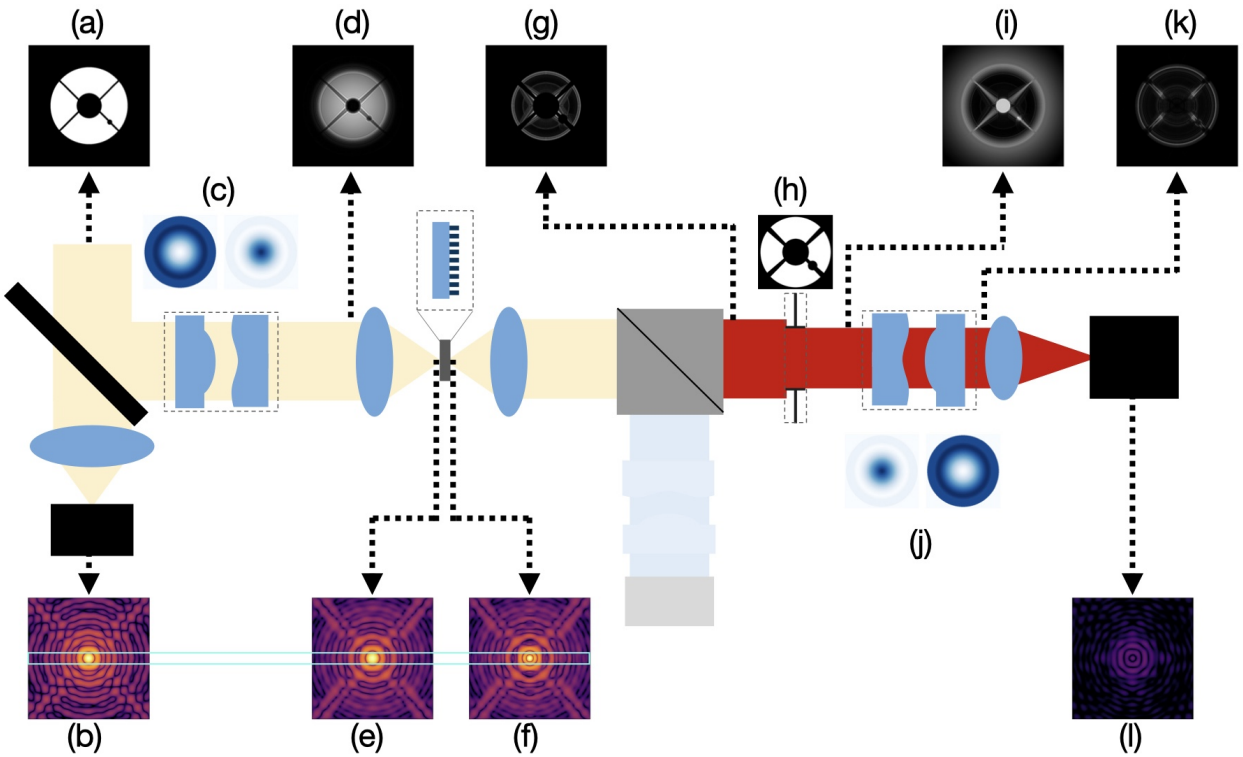


Figure 4.1: Schematic of the optical setup used in the simulation, with pupil-plane images shown on the top, optical components in the middle section, and focal-plane images in the bottom row. The pupil-plane light after the MagAO-X aperture stop is shown in (a), with the corresponding unaberrated point spread function (PSF) in (b) for reference. The light then passes through a pair of PIAA lenses, whose radial profiles are shown in (c), producing the apodized pupil-plane image in (d). Next, the light is focused onto the focal plane mask (FPM), with panels (e) and (f) showing the PSFs before and after the FPM, respectively. The teal box spanning across the focal-plane images (b), (e), and (f) highlights how the PIAA lenses enlarge the PSF core between (b) and (e), and how the FPM introduces a phase shift across the PSF core, leading to interference that redistributes the energy from the central core into a secondary ring structure. Note that only the coronagraphic channel is illustrated here; thus, the PSF in (f) corresponds to the redder light. Because the FPM is a transmissive phase mask, it does not significantly change the PSF intensity between (e) and (f) but instead alters the phase of the core region. The relayed pupil-plane image from the FPM is shown in (g). The beam then passes through the Lyot stop, designed for MagAO-X, shown in (h), which blocks the light diffracted by the FPM, resulting in the pupil-plane image in (i). Subsequently, the light propagates through a set of inverse-PIAA lenses, whose radial profiles are shown in (j). These lenses restore the pupil to its original form, as seen in the pupil image (k), which is then focused onto the coronagraphic camera to produce the final coronagraphic PSF shown in (l).

therefore used, following the design from Foster, 2023. Figure 4.1 summarizes the optical setup used for evaluating the metasurface-based FPMs. The top row shows key pupil-plane images, while the bottom row shows the corresponding focal-plane intensity distributions throughout the optical train. The system has an effective focal ratio of $f/69$. From this point onward, all focal-plane

coordinates are expressed in units of $\lambda/D$, where the focal length ($f$) is absorbed in.

**Simulation framework**

The optical simulations were implemented in Python using the HCIPy (High Contrast Imaging for Python) package (E. H. Por et al., 2018). The input pupil was defined by fixing the spatial sampling across the telescope aperture based on the desired grid resolution and physical pupil diameter. The simulation used $2^8 \times 2^8$ pixels across a grid extending 1.5× the telescope aperture size to avoid wrap-around effects from the FFT-based propagation. The MagAO-X aperture, including the central obscuration and support structures, was modelled as a binary transmission map and applied to the pupil using the `Field` class. The 6.5 m telescope pupil was numerically scaled to the instrument beam diameter of 8.9 mm.

Two focal-plane grids were defined. The first, representing the science detector, spanned 15×15 $\lambda/D$ with 30 pixels per $\lambda/D$. A second finer grid was made that matched the physical extent of the FPM (typically 1.1–1.8 $\lambda/D$ in diameter in this work) and used $2^8 \times 2^8$ pixels to capture detailed substructure from the metasurface design. The propagation between pupil and focal planes was handled using the `FraunhoferPropagator`, which computes scalar diffraction in the far-field approximation.

The PIAA and inverse-PIAA lenses were modelled using the `SurfaceApodizer` class, which allows specifying a surface sag profile and refractive index to compute the corresponding optical path difference. The lens sag profiles, derived from the MagAO-X design (Foster, 2023), were interpolated onto the simulation grid. A custom `PIAAChain` class was implemented to handle sequential propagation through the PIAA pair using `AngularSpectrumPropagator` objects, with a propagation distance of 60.2 mm between the two lens surfaces and 37.2 mm between the pupil plane and the first (or second, in the case of the inverse-PIAA) lens. This approach accurately models the near-field diffraction between the refractive surfaces and their inverse counterparts.

To include the metasurface-based FPMs, a modified version of the HCIPy `ZernikeWavefrontSensorOptics` class was developed. This new class, named `modified_focalPlaneMaskOptics`, allows the phase and amplitude distributions of an arbitrary FPM to be directly imported as complex fields from full-wave FDTD simulations. The class uses the `Apodizer` object to apply the complex mask transmission and the `FraunhoferPropagator` for field propagation to and from the focal plane. This flexible implementation enables the same class to be used for any custom focal-plane optic where an arbitrary complex transmission needs to be applied. It additionally can also handle arbritary phase step and amplitude step float values to create custom ideal FPM without any abberations.

The input light was defined using the `Wavefront` class from the initial pupil plane field, with

optional low-order aberrations introduced via a power-law phase screen generated by the `make_power_law_modified` function. The optical elements were then sequentially applied to the wavefront following the system layout described in Fig. 4.1. Each propagation step—through the PIAA lenses, FPM, Lyot stop, and inverse-PIAA optics was carried out using the defined propagators, producing the simulated pupil- and focal-plane field distributions. The resulting complex field was then used for image formation and subsequent analysis for coronagraphic and wavefront-sensing performance. The end-to-end code used for this can be found on Patel and S. Haffert, 2025.

Using this simulation framework, the metasurfaces can now be evaluated as focal-plane masks (FPMs) for both coronagraphy and wavefront sensing. Specifically, the first step is to determine the optimal mask size that maximizes coronagraphic performance, followed by evaluating the wavefront-sensing performance at that same mask size.

## 4.2 The coronagraphy arc

To evaluate the coronagraphic performance of the system, consisting of the focal plane mask (FPM) and the Lyot stop, the main metric considered is the contrast, defined as the residual starlight remaining in the coronagraphic image (Kenworthy and S. Y. Haffert, 2025). Since the goal is to measure how effectively the FPM suppresses on-axis starlight, only an on-axis source is propagated through the optical system for this calculation. The contrast is defined as the ratio of the peak flux in the coronagraphic image (with FPM + Lyot Stop) to that in the corresponding non-coronagraphic image.

To measure the throughput for off-axis planet light, a simulated off-axis source is propagated, and the throughput is calculated as the ratio of the total flux in the coronagraphic image to that in the non-coronagraphic image. The inner working angle (IWA) is defined as the angular separation where the throughput drops to half of its maximum value.

The optimal mask diameter, expressed in units of $\lambda/D$, is determined for both metasurface FPMs: the cuboidal and cylindrical designs[1]. The complex transmission maps obtained from the FDTD simulations (see Fig. 3.11 for the maps) are used for this evaluation. In addition, idealized versions of the FPMs are analyzed using their mean amplitude and phase values to separate the effects of finite-size simulation artifacts from the intrinsic optical response of the metasurface.

### Optimal mask size

The peak contrast in the coronagraphic image as a function of the mask size for the cuboidal and cylindrical metasurface (MS) FPMs are shown in Fig. 4.2. For both metasurface geometries, the

[1] From now on will be referred to as Cuboidal and Cylindrical metasurface (MS)

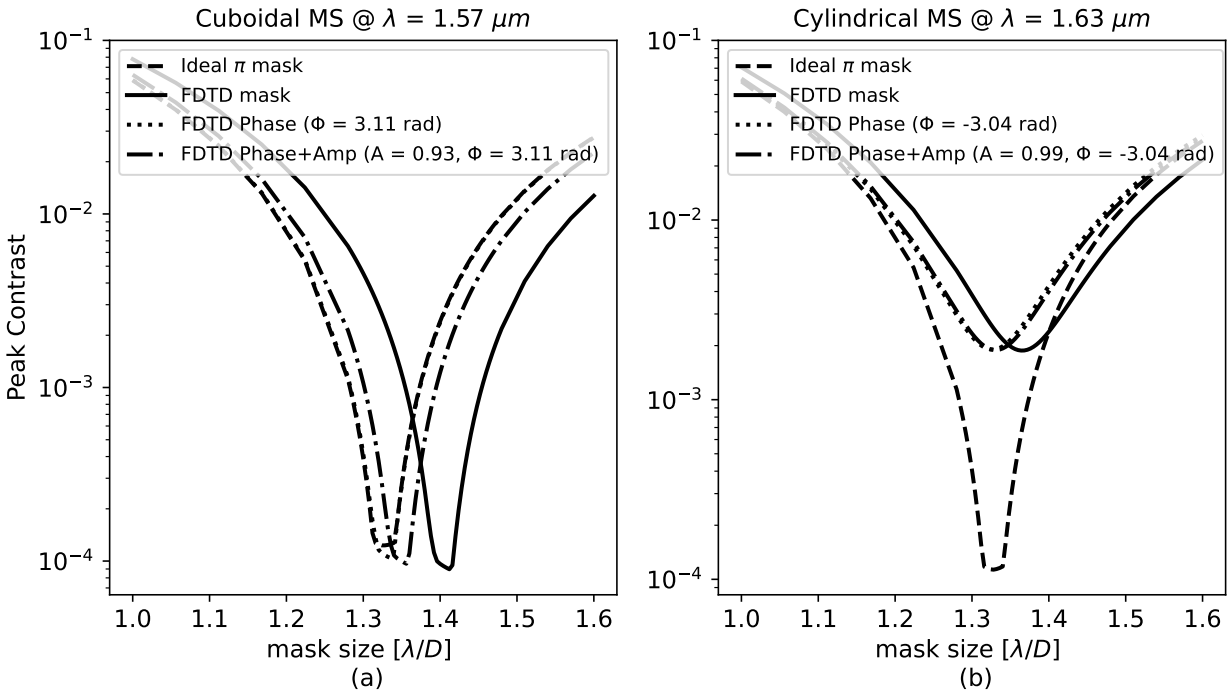


Figure 4.2: Peak contrast performance of the cuboidal and cylindrical metasurface (MS) focal-plane masks (FPMs) as a function of different mask diameter in units of $\lambda/D$. Each plot compares the contrast curves for the ideal $\pi$ mask, the full complex transmission from the FDTD simulation, and simplified versions using only the mean phase or the combined mean phase and amplitude values. The results for the cuboidal MS at $\lambda = 1.57\,\mu$m are shown in (a), and those for the cylindrical MS at $\lambda = 1.63\,\mu$m are shown in (b). The optimal mask diameter corresponds to the minimum of each contrast curve, with the non-ideal transmission amplitude and phase from the FDTD simulations shifting the contrast minimum slightly relative to the ideal $\pi$ mask case.

overall trend follows that of the ideal $\pi$ mask, where the contrast initially improves with increasing mask size, reaches a minimum near the optimal value, and then degrades for larger diameters. For the cuboidal MS, the optimal mask diameter occurs at approximately 1.41 $\lambda/D$ for the full FDTD-derived mask, while the ideal $\pi$ mask reaches its minimum contrast at 1.32 $\lambda/D$. When only the mean phase from the FDTD simulation is used, the optimal value shifts to 1.34 $\lambda/D$, and including both the mean amplitude and phase yields a minimum at 1.36 $\lambda/D$. Similarly, for the cylindrical MS, the optimal mask diameters for the full FDTD, phase-only, and phase–amplitude cases occur at 1.36 $\lambda/D$, 1.33 $\lambda/D$, and 1.33 $\lambda/D$, respectively. These values are summarized in Table 4.1.

The deviations between the ideal and FDTD-derived cases can be attributed to differences in both the phase shift and transmission amplitude of the metasurfaces relative to their target values of $\pi$ and unity, respectively. For the cuboidal MS, the mean phase shift and amplitude obtained from the FDTD simulations are $\Phi = 3.11$ rad and $A = 0.93$ (corresponding to transmission $T = A^2 \approx 0.86$),

| Configuration | FDTD Mask | FDTD Φ | FDTD Φ + A |
|---|---|---|---|
| Cuboidal MS @ 1.57 $\mu$m | 1.41 | 1.34 | 1.36 |
| Cylindrical MS @ 1.63 $\mu$m | 1.36 | 1.33 | 1.33 |

Table 4.1: Optimal mask diameters (in units of $\lambda/D$) corresponding to the minimum contrast for different FPM cases.

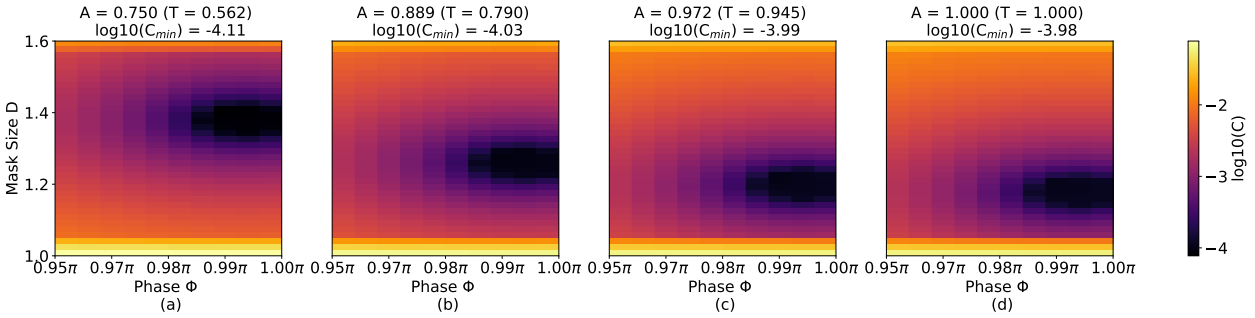


Figure 4.3: Contrast maps showing the dependence of the coronagraphic performance on the mask phase shift ($\Phi$) and mask diameter ($D$) for different fixed transmission amplitudes ($A$). Each panel corresponds to a different amplitude value, with the associated intensity transmission ($T = A^2$) and minimum contrast value $\log_{10}(C_{\min})$ indicated above. The phase shift is varied between $0.95\pi$ and $1.00\pi$, and the mask diameter between $1.0\,\lambda/D$ and $1.6\,\lambda/D$. The color scale represents $\log_{10}(C)$, where darker regions correspond to lower contrast values. Note to isolate the effect of the mask, no PIAA-iPIAA lens were included.

while for the cylindrical MS they are $\Phi = 3.04$ rad and $A = 0.99$ ($T \approx 0.98$). The achievable contrasts at their respective optimal mask sizes are approximately $\sim 10^{-4}$ and $\sim 10^{-3}$, respectively. Although one might expect that a lower transmission (i.e., a more opaque mask) could improve starlight suppression, the results clearly show that this is not the case—the ideal $\pi$ mask, which is fully transmissive, still provides the best overall contrast. This behavior highlights that the contrast degradation is primarily driven by phase deviations from the target $\pi$ shift, rather than by amplitude losses. As expected, the phase response of the metasurface plays the dominant role in setting the achievable null depth, consistent with the phase-sensitive nature of destructive interference in coronagraphic suppression (F. Roddier and C. Roddier, 1997). To more clearly isolate and visualize the relative influence of phase and amplitude deviations, a full 3D parameter scan was performed, mapping contrast as a function of both parameters with the inclusion of PIAA lens.

Fig. 4.3 shows the resulting contrast maps, where each panel corresponds to a different transmission amplitude. The contrast minimum consistently occurs near a $\pi$ phase shift, with only a weak negative correlation with amplitude over the range tested ($A = 0.75$–$1.0$), where lower amplitudes yield slightly better contrast simply because the FPM becomes more opaque. It should be noted that very low transmission amplitudes are not desirable, as they would reduce the overall throughput of the

system. More importantly, the results highlight how variations in transmission amplitude influence the optimal mask size: lower transmission amplitudes shift the optimal size toward larger diameters. This likely occurs because when the mask transmits less light, a larger area is required to maintain sufficient $\pi$-shifted light for effective destructive interference. Although further investigation is needed to confirm this explanation, the key takeaway is that such metasurface-based FPMs require highly accurate phase realization to achieve the desired contrast, and deviations in transmission amplitude can affect the effective optimal mask size.

### Contrast and throughput performance

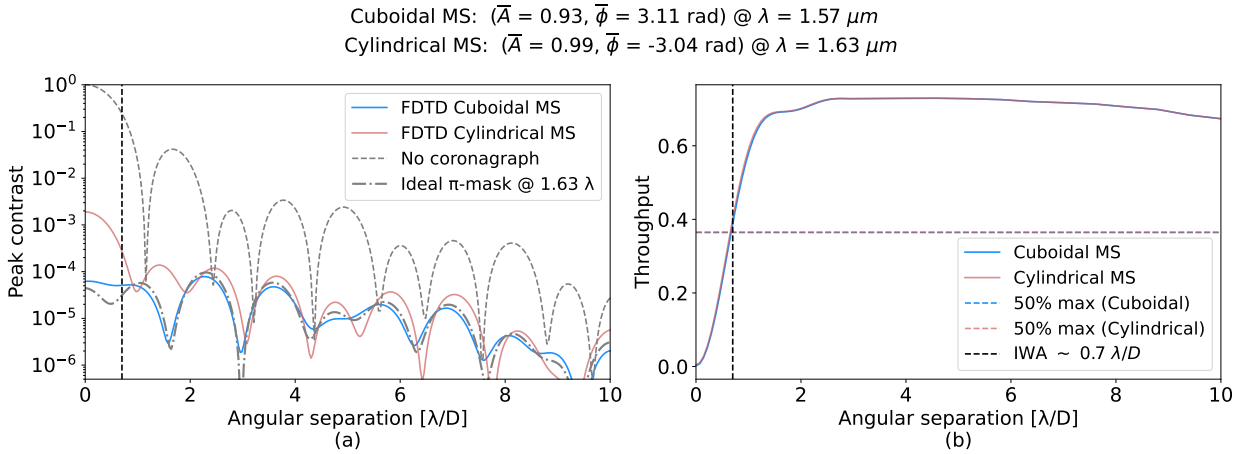


Figure 4.4: Peak contrast and throughput performance of the metasurface (MS) focal-plane masks (FPMs) at their optimal sizes. The contrast curves are in (a) for the cuboidal MS at $\lambda = 1.57\,\mu$m and the cylindrical MS at $\lambda = 1.63\,\mu$m are shown together in blue and red curves. The two gray curves show the contrast for the ideal $\pi$ mask and non-coronagraphic response in dotted-dashed and dashed curves, respectively. (b) shows the throughput as a function of angular separation for both metasurfaces. Both curves has maximum values of $\sim 70\%$. The horizontal dashed line denote the 50% of maximum throughput levels used to define the inner working angle (IWA), indicated by the vertical black dashed line.

The contrast and throughput curves in Fig. 4.4 show the on-axis suppression and off-axis transmission performance of the metasurface FPMs, respectively. The cuboidal MS reproduces coronagraphic behavior nearly identical to that of the ideal $\pi$ mask, achieving a peak contrast of $\sim 10^{-4}$, with its diffraction pattern closely overlapping the ideal case beyond the first bright ring. This performance is attributed to its near-ideal phase shift of $3.11, \text{rad}$. In contrast, the cylindrical MS exhibits a lower peak contrast of $\sim 10^{-3}$ due to its non-ideal phase of $-3.04, \text{rad}$, though its diffraction pattern remains comparable beyond the second bright ring. Both metasurfaces show identical throughput and thus the same IWA, as the throughput is primarily limited by the Lyot stop. Overall, the metasurface design with a phase response closer to the ideal value demonstrates superior contrast performance, while maintaining equivalent off-axis throughput and IWA. But the

contrast profiles for both stays below $\lesssim 10^{-4}$ beyond the the IWA.

### 4.3 The wavefront-sensing arc

**Sensitivity to photon noise**

Having assessed the coronagraphic performance we now look at how the focal-plane mask behaves as a wavefront sensor (WFS). Since we optimize the properties of mask (such as size) for optimal coronagraphic performance, it is important to be more critical of the wavefront sensing. Specially, the dynamic range, the sensitivity to photon-noise and its effect on the reconstruction is assesed.

The WFS uses intensity measurements to reconstruct the incoming wavefront, either with linear methods such as Eq. 2.22 and the method of (Mamadou N'Diaye et al., 2013), or with more recent non-linear approaches based on gradient descent (S. Y. Haffert, 2024) and with backpropagation (Haffert, Deo, and Chambouleyron (in prep.)). Because these reconstructions depend directly on measured intensities, it is important to understand how noise affects them. One way is to evaluate how photon noise contributes to the standard deviation of the reconstruction error (S. Y. Haffert, 2024).

Another way to express the sensitivity is through the Fisher information (FI) of each phase mode under photon noise (S. Y. Haffert, Males, and Olivier Guyon, 2023). The FI is directly related to sensitivity because it quantifies how strongly the detected photon distribution changes in response to small variations of a phase mode, and the Cramér–Rao lower bound converts this into the minimum achievable estimation variance. FI provides a fundamental measure of measurement accuracy for photon-limited wavefront sensing. Thus, a larger FI directly implies a more sensitive measurement, with lower estimator variance. For starlight (an incoherent pupil source), the classical Fisher information can saturate the quantum Fisher information bound of 4 for all non-piston modes (S. Y. Haffert, Males, and Olivier Guyon, 2023), setting the absolute upper limit on wavefront-sensing sensitivity. This maximum is achieved when the sensor produces maximum phase contrast between the perturbed and unperturbed fields, which is when the input profile matches the profile of the mask (Paterson, 2008; S. Y. Haffert, Males, and Olivier Guyon, 2023).

To calculate the Fisher information for a given mode, consider the phase expressed as a modal expansion,

$$\phi(\mathbf{r}) = \sum_n \phi_n \, w_n(\mathbf{r}), \tag{4.1}$$

where $\phi_n$ is the coefficient of mode $n$ and $w_n$ is its spatial basis function. The incoming field is then

$$E_{\text{in}} = A \exp\left( i \sum_n \phi_n w_n \right). \tag{4.2}$$

The derivative of $E_{\text{in}}$ with respect to the (scalar) phase coefficient is obtained using the chain rule,

$$\frac{\partial E_{\text{in}}}{\partial \phi_n} = A\, i w_n \, \exp\left( i \sum_j \phi_j w_j \right) = i\, w_n\, E_{\text{in}}. \tag{4.3}$$

This expresses how the electric field changes when the coefficient of mode $n$ is perturbed.

Propagation through the optical system is represented by a linear operator $C$, so

$$\frac{\partial E_{\text{out}}}{\partial \phi_n} = C\left[ \frac{\partial E_{\text{in}}}{\partial \phi_n} \right] = C\left[ i\, w_n E_{\text{in}} \right]. \tag{4.4}$$

We define the propagated modal field

$$E_n := C\left[ w_n E_{\text{in}} \right], \tag{4.5}$$

which allows the field derivative to be written compactly as

$$\frac{\partial E_{\text{out}}}{\partial \phi_n} = i\, E_n. \tag{4.6}$$

The WFS measures intensity,

$$I = |E_{\text{out}}|^2, \tag{4.7}$$

so the derivative with respect to the modal coefficient is (Jurling and Fienup, 2014)

$$\frac{\partial I}{\partial \phi_n} = 2\, \Re\left( E_{\text{out}}^* \frac{\partial E_{\text{out}}}{\partial \phi_n} \right) = -2\, \Im\left( E_{\text{out}}^* E_n \right). \tag{4.8}$$

Under photon noise, the Fisher information for mode $n$ is

$$\text{FI}_n = \int \frac{1}{I} \left( \frac{\partial I}{\partial \phi_n} \right)^2 ds, \tag{4.9}$$

and substituting Eq. 4.8 yields

$$\text{FI}_n = 4 \int \left[ \Im\left( \frac{E_{\text{out}}^* E_n}{|E_{\text{out}}|^2} \right) \right]^2 ds \tag{4.10}$$

The photon-noise sensitivity is the square root of the Fisher information. This follows from the Cramér–Rao bound, which states that the minimum achievable standard deviation on an unbiased estimator of the mode coefficient is $\sigma_n = 1/\sqrt{\text{FI}_n}$.

We use a Fourier modal basis, so each phase mode corresponds to a single spatial frequency on the pupil (in cycles per pupil, cpp). Low frequencies represent slowly varying aberrations, while high

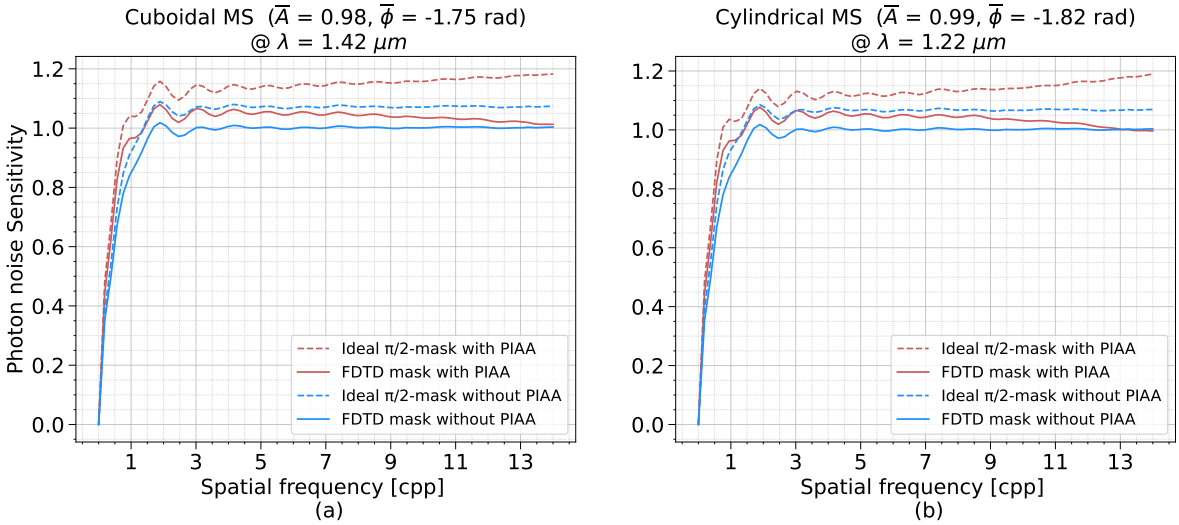


Figure 4.5: Photon-noise sensitivity performance of the metasurface (MS) based FPMs as a function of spatial frequency at optimal coronagraphic mask size. Results for the cuboidal MS at $\lambda = 1.42\,\mu$m are shown in (a), and for the cylindrical MS at $\lambda = 1.22\,\mu$m in (b). Each panel compares the FDTD-simulated mask (solid lines) with an ideal $\pi/2$-mask (dashed lines), both with PIAA optics (red curves) and without PIAA (blue curves).

frequencies correspond to rapidly varying phase structure. Photon noise itself does not depend on spatial frequency, but the WFS response does, different modes produce different amounts of intensity change in the sensor. The Fisher information, the amount of information each photon carries depends on the intensity. And therefore the photon-noise sensitivity varies with spatial frequency and ideally a good wavefront sensor would have higher sensitivity throughout all the spatial frequencies over 1.

Figure 4.5 shows the photon-noise sensitivity as a function of spatial frequency for the two FPMs designs at the mask size where the coronagraphic performance is optimized (see table 4.1). Each panel compares the performance of the FDTD-simulated metasurface mask against an ideal $\pi/2$ mask (ZWFS), both with and without the inclusion of the PIAA optics. In all cases, the sensitivity rises rapidly at very low ($< 1.5$[cpp]) spatial frequency and then plateaus around after $\sim 2$ cpp. The ideal case reach a maximum of $\sim 1.15$ compared to 1.05 for the two FDTD masks. The PIAA optics also the improve sensitivity (by $\sim 7\%$) for all the cases. This is because with PIAA the profiles between the mask (airy pattern) and the incoming field (top-hat profile) can be matched by apodizing the field (S. Y. Haffert, Males, and Olivier Guyon, 2023; Chambouleyron, Fauvarque, Plantet, et al., 2022). Interestingly the PIAA with ideal masks tends to increase the sensitivity at higher frequencies while decrease for the simulated mask. More investigation is required to understand the underlying reason for this trend.

While the size of the FPM is fixed by the optimal coronagraphic performance, it is still informative

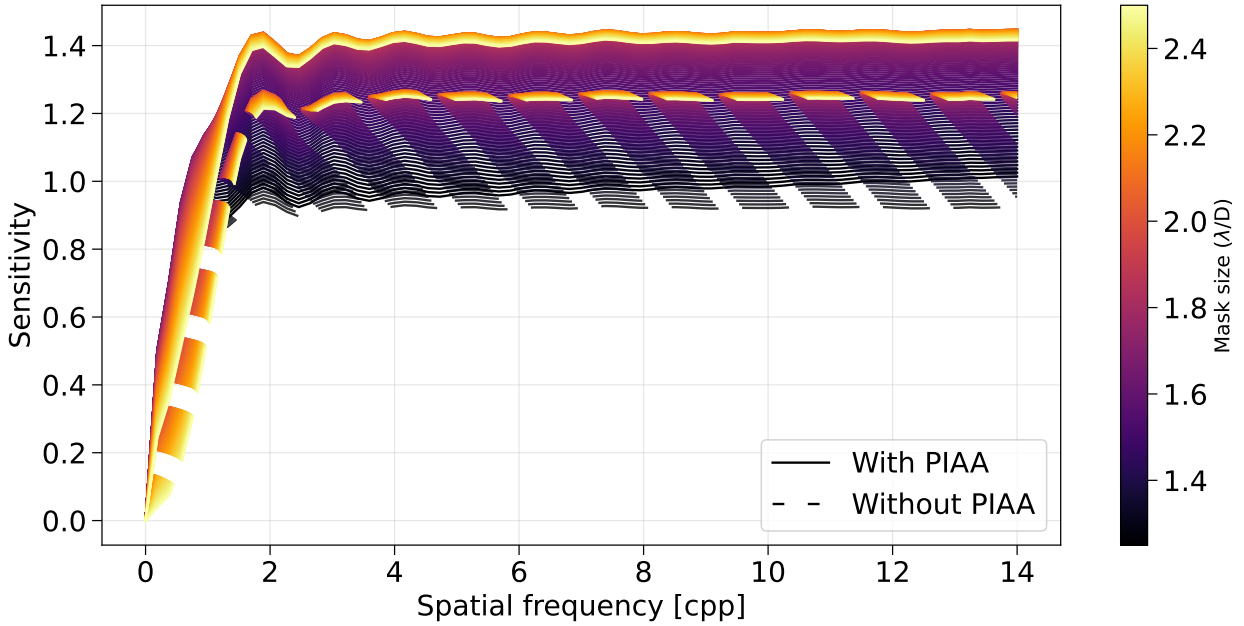


Figure 4.6: Photon noise sensitivity of an ideal FPM ($\Phi = \pi/2$, A=1) at different mask size with and without PIAA-iPIAA setup. Sensitivity as function of spatial frequency (in cpp) with and without PIAA-iPIAA setup in solid and dashed line respectively. The color of the line indicates the mask size and indicated by the colorbar over the range of 1.25 to 2.50 $\lambda$/D.

to examine how the photon-noise sensitivity varies with mask diameter. Figure 4.6 shows the sensitivity curves for an ideal $\pi/2$ mask across a range of mask sizes. Although the overall behavior of the curves follows the trend described earlier, the main change with mask size is the overall sensitivity level. As seen in Fig. 4.6, the sensitivity reaches its maximum near the expected optimal size of $\sim 2\,\lambda$/D. This is consistent with the results of Chambouleyron, Fauvarque, Jean-François Sauvage, et al., 2021 for an ideal ZWFS phase dot. In our case, however, the peak sensitivity slightly is $\sim 1.44\,\lambda$/D compared to $\sim 1.75\,\lambda$/D) in that study. This may be due to the complex telescope pupil geometry used here compared to a clear aperture. The PIAA lenses were designed to optimize coronagraphic performance (Foster, 2023), not wavefront sensor sensitivity. Having said that, the highest sensitivity is still achieved when the PIAA optics are included for this pupil.

**Wavefront reconstruction and Dynamic Range**

Now, the wavefront sensor's ability to reconstruct aberrated phase screens is explored. The input phase aberrations were generated from a power-law power spectral density (PSD) of the form $\mathrm{PSD}(f) \propto f^{-\beta}$, where $f$ is the spatial frequency, and $\beta$ sets the slope of the spectrum. The input root-mean-square (rms) (or standard deviation, since the mean is $\sim 0$ rad) of the screen and the exponent ($\beta$) of the PSD are defined. The aberration is calculated on the same telescope pupil grid

defined for the simulation, and the aberrated phase is applied to the flat wavefront.

Firstly, the linear reconstructor was explored. The linear ZWFS reconstruction relation is derived in (Eq. 2.22), which provides a first–order estimate of the pupil-plane phase from the measured ZWFS intensity. Using this expression, we implemented a linear reconstructor that operates directly on the simulated ZWFS outputs. The implementation computes the unaberrated field, the reference field, and the differential intensity, and then applies the linear formula to recover the phase. Piston is removed from the reconstructed phase by subtracting the median inside the telescope pupil.

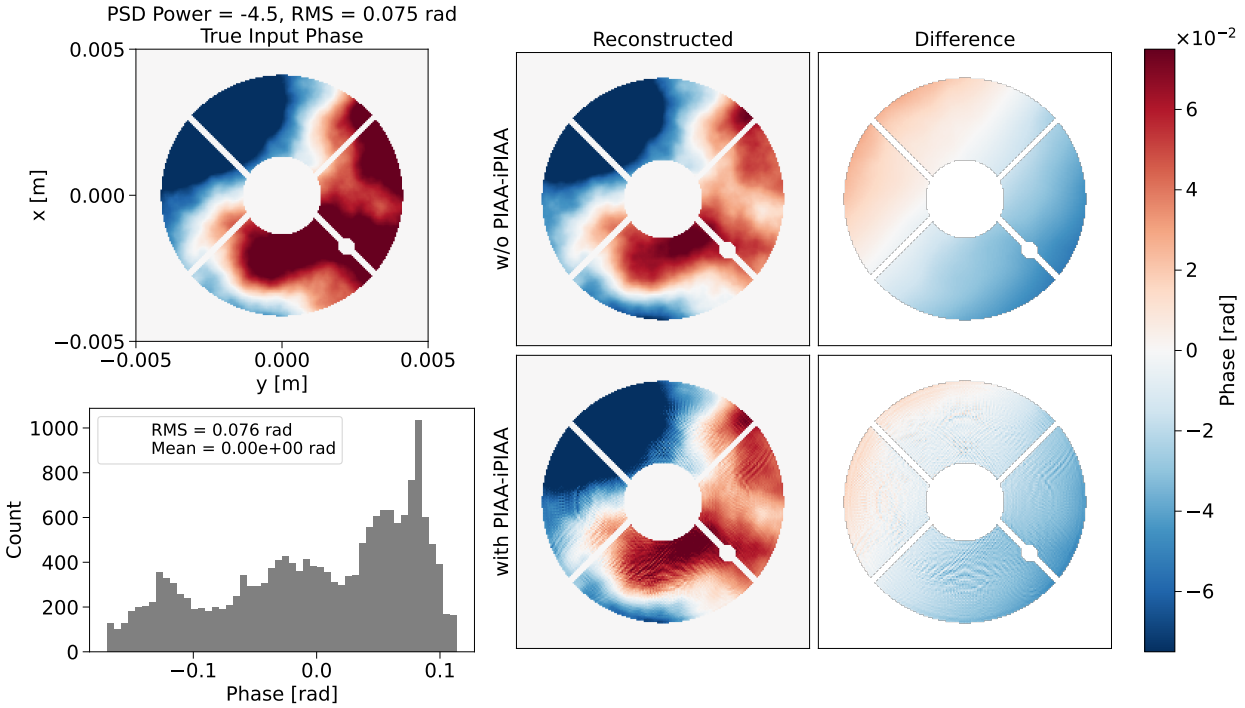


Figure 4.7: Implementation of the linear reconstructor for systems with and without the PIAA–iPIAA optics. The left panel, top row, shows the true input phase aberration within the pupil with input rms of 0.1 rad and a PSD power of −4.5. The bottom row shows the distribution of the phase inside the pupil with the measured rms and mean. The right panels show the reconstructed phase (middle column) and the residual difference (right column). Results without PIAA–iPIAA are shown in the top row, and results with PIAA–iPIAA in the bottom row. All phase maps share the common colorbar on the right.

Figure 4.7 shows an example reconstruction for a phase screen with an rms of 0.1 rad and a PSD power of −4.5. The true input phase inside the pupil and the distribution of the phase are shown to validate the generation of phase screens. The reconstructed phase and the residual difference are shown on the right for both systems. The linear reconstructor successfully recovers the large-scale structure of the aberration in both cases, confirming that it behaves as expected for small phase errors.

However, there are noticeable high-spatial-frequency artifacts in the reconstruction when the PIAA–iPIAA optics are included. These small-scale features arise from numerical structure in the forward model—mainly related to the remapping optics—and the linear approximation does not capture their contribution accurately with a finite number of pixels. In principle, this can be mitigated by using a much finer grid than $2^8 \times 2^8$, but this would significantly increase the computation cost in the Monte Carlo simulations. The linear reconstructor in Chapter 2.2 was derived with the aim of modeling these artifacts, since commonly used approaches such as Mamadou N'Diaye et al. (2013) use only the differential intensity and the angular component (phase) of the field for reconstruction, which are more practical for implementation. While the linear reconstructor performs better with these numerical artifacts, they remain significant enough that high-frequency errors accumulate over time and will not converge when used in closed loop.

Because of this, we use a non-linear reconstructor, which can capture the full model of the optical system. Moreover, using a non-linear reconstruction can increase the dynamic range (S. Y. Haffert, Males, and Olivier Guyon, 2023). In Haffert, Deo, and Chambouleyron (in prep.), they demonstrated a non-linear reconstructor based on an iterative forward–backward propagation framework for any arbitrary linear optical system. The same method is used in this thesis, where each iteration begins by forward-propagating the estimated wavefront through the optical system and comparing its predicted intensity to the measurement. Using that measurement and a designated cost function, the change in the electric field is computed. This correction is then back-propagated and projected onto the wavefront-sensor pixel basis, allowing for a gradient-descent-based update that gradually refines the wavefront estimate until convergence. To minimize the cost function, `scipy`'s `minimize` function was used with the bounded limited-memory BFGS (L-BFGS-B) method.

Firstly, a convergence test was performed to estimate how many iterations the non-linear reconstructor requires to reconstruct the wavefront to machine precision of $\sim 10^{-15}$–$10^{-16}$ for 64-bit double precision. We compared the steps taken for the system with and without the PIAA–iPIAA setup for an ideal ZWFS at a $\sim 1.4\,\lambda/D$ mask size. Figure 4.8 shows the convergence curves for different input rms values with a PSD power of $-0.5$. The choice of a shallower PSD power was to create small-scale variations that are more difficult to reconstruct. This provides a conservative estimate of the required number of iterations. For smaller input rms cases of 0.1, 0.01, and 0.001 rad, the reconstruction error converges to machine precision for both systems. Specifically, it takes $\sim$ 20–40 iterations without the PIAA–iPIAA optics, depending on the input rms, and $\sim$ 130–150 iterations when they are included. For an input rms of 1 rad, the reconstructor does not converge due to phase wrapping, as the peak-to-valley difference exceeds $\pi$, making the phase ambiguous. Hence, it would take $\sim$ 150 iterations for the non-linear reconstructor to converge to a solution

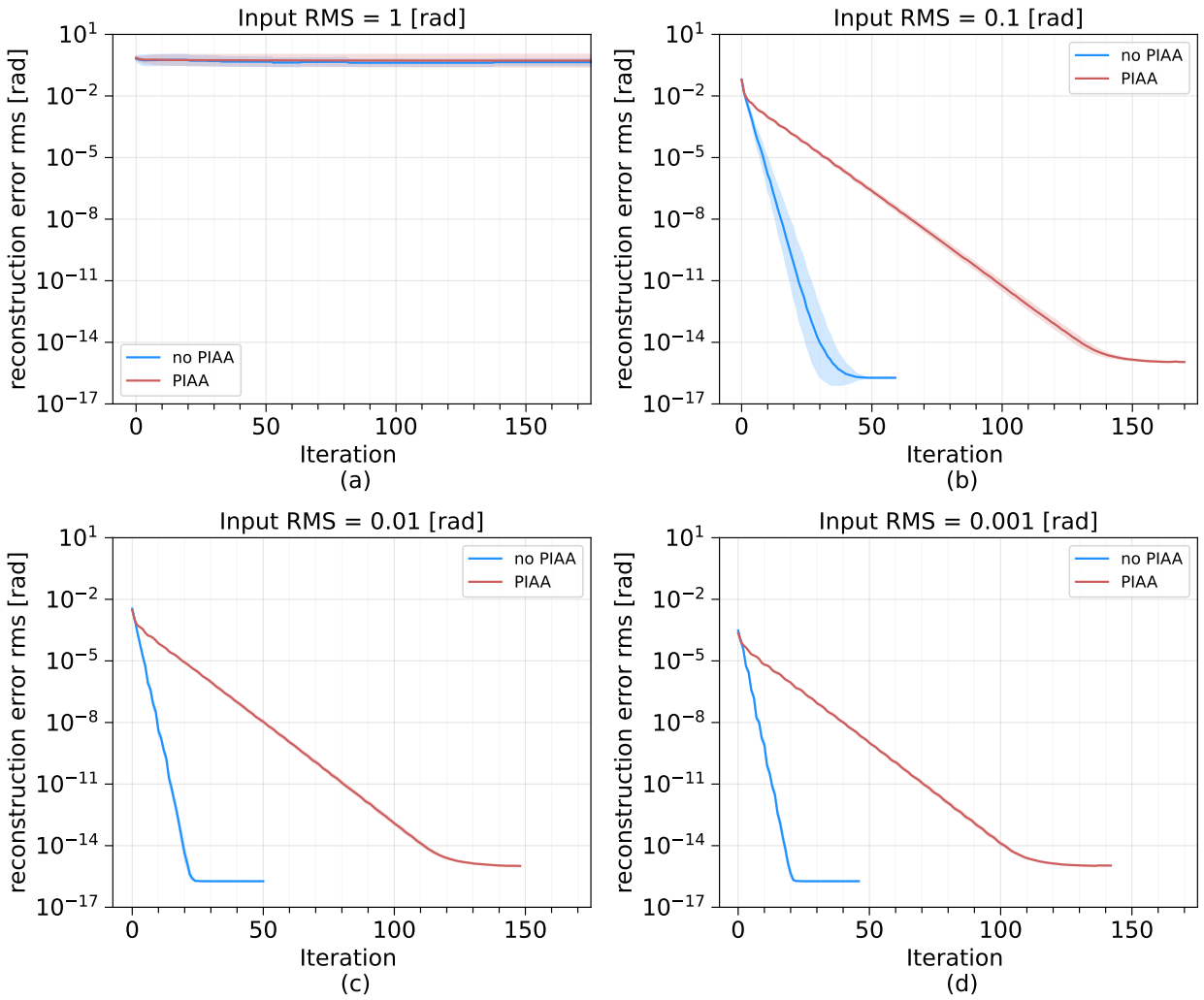


Figure 4.8: Convergence test for the non-linear reconstructor. The plots show the reconstruction error (rms, in log scale) as a function of iteration number for different input phase rms values: 1, 0.1, 0.01, and 0.001 rad in panels (a), (b), (c), and (d), respectively. In all cases the input phase follows a PSD power law of −0.5. The blue curves correspond to the system without PIAA–iPIAA optics, and the red curves correspond to the system with PIAA–iPIAA included.

where the difference is essentially at machine precision. However, performing this many iterations is computationally expensive, and in a closed-loop system the iterations naturally converge over time. Therefore, for the dynamic range study, the maximum number of iterations is limited to 50, for which the minimum achievable reconstruction error is $\sim 10^{-7}$–$10^{-6}$.

To quantify the dynamic range of the system, we performed a Monte Carlo test using 50 random phase screens for each input rms between $10^{-4}$ and $10^{0}$ rad. Each screen follows a PSD power law of −4.5 and was reconstructed using the non-linear solver (up to 50 iterations) for the ideal ZWFS mask, the cuboidal metasurface mask, and the cylindrical metasurface mask. The results are shown

in Fig. 4.9, which plots the mean reconstruction error rms as a function of the input rms for the three masks, with the shaded regions indicating the $1\sigma$ spread over the Monte Carlo trials. All three masks behave similarly at very small input rms values, where the reconstruction error stays nearly flat, indicating that the non-linear solver is operating in its ideal regime. The performance begins to change once the input rms increases beyond $\sim 0.25$–$0.45$ rad, after which the error for all masks grows steadily as the solver approaches the limit of its dynamic range. Although the metasurface masks show slightly larger mean errors than the ideal $\pi/2$ mask at the highest input rms values, the overall scaling behavior remains essentially the same, with the standard-deviation bands of all curves overlapping. All three masks therefore display comparable dynamic-range performance across the full tested range.

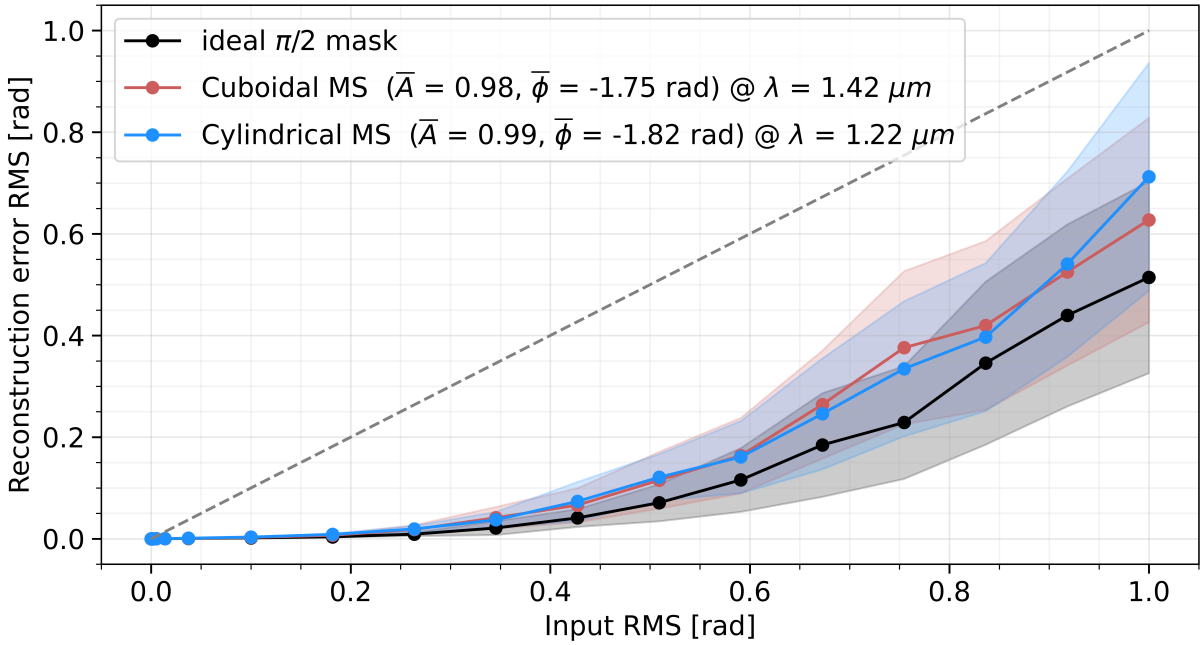


Figure 4.9: Dynamic range of the designed FPMs. Mean reconstruction error rms as a function of input rms for the ideal ZWFS, cuboidal, and cylindrical metasurface masks (black, red, and blue curves, respectively) shown over the Monte Carlo trials. The shaded region shows the $1\sigma$ spread.

**Effect of photo noise on reconstruction**

It is also interesting to study the reconstruction performance under photon-noise. Since the dynamic range of the two MS were comparable, for this exercise only the cuboidal MS (designed for 1.42 $\mu$m) was used. A sample of 10 phase screens with input 0.1 and 0.01 [rad] and PSD exponent of $-4.5$ was used. The measured intensity on a $2^8 \times 2^8$ pixel grid from the wavefront sensor was converted into expected photon counts, from which noisy photon arrivals were drawn from a Poisson distribution. These counts were then normalized by $N_\gamma$ to obtain the noisy intensity distribution. A range of

$N_\gamma = 10^2 - 10^{23}$ was used.

As seen from Fig. 4.10, the reconstruction error follows the expected photon-noise–limited trend, decreasing approximately as $N_\gamma^{-1/2}$ for both input RMS levels. In this regime, each additional order of magnitude in photon number improves the reconstruction accuracy by roughly a factor of three, demonstrating that the PIAA–iPIAA architecture operates in the shot-noise–dominated limit at low photon counts.

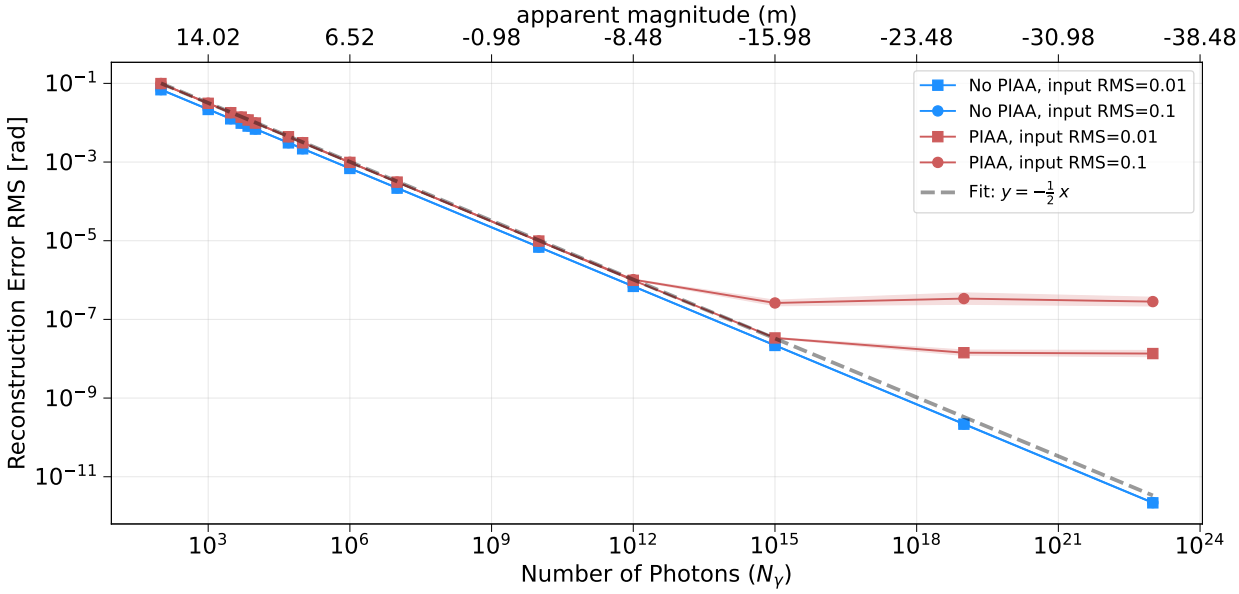


Figure 4.10: Photon-noise–limited wavefront reconstruction with the PIAA–iPIAA setup with the cuboidal MS at 1.42 $\mu$m. Reconstruction error RMS using a non-linear reconstructor with photon noise for different numbers of photons, with input RMS values of 0.1 and 0.01 shown in circle and square scatter-point blue curves, respectively. The dashed line shows a fitted line with a slope of $-0.5$ for the PIAA curves. The top x-axis shows the corresponding apparent magnitude following Equation 4.12. The blue curve shows the same but for setup without PIAA-iPIAA for reference.

Beyond $N_\gamma \sim 10^{12}$–$10^{15}$ (depending on the input RMS), however, the reconstruction error departs from the photon-noise scaling and begins to plateau. This behaviour arises entirely from capping the non-linear reconstructor to 50 iterations. From Fig. 4.8(b) and (d), we see that after 50 iterations the reconstruction error RMS (with PIAA) reaches $\sim 10^{-7}$ rad and $\sim 10^{-8}$ rad for input RMS values of 0.1 rad and 0.01 rad, respectively. The same plateau levels appear in Fig. 4.10, confirming that the flattening of the curves is a numerical consequence of the iteration limit rather than a physical limitation of the WFS. In principle, the reconstruction error RMS would continue to decrease with increasing photon number if more iterations ($\sim$ 150) were allowed, or when operated in closed loop, eventually reaching machine precision.

The photon-noise–limited performance directly informs about the type of star that can be observed

with the system. For an estimate, the apparent magnitude was calculated from $N_\gamma$ using

$$N_\gamma = T\, F_0\, 10^{-m/2.5}, \tag{4.11}$$

where $T = 0.3$ is the total system throughput and

$$F_0 = 2.14 \times 10^9 \,\text{photons}\,\text{s}^{-1}\,\text{m}^{-2}\,\mu\text{m}^{-1}$$

is the monochromatic zero-magnitude photon flux at $\lambda = 1.42\,\mu$m. Solving this expression for $m$ gives the final approximate relation used further in this exercise,

$$m = 21.52 - 2.5\log_{10}(N_\gamma). \tag{4.12}$$

Using this relation, the photon counts can be mapped onto an equivalent apparent magnitude scale to give a sense of the stellar brightness associated with the photon-noise–limited regime. The apparent magnitudes shown in the Fig 4.10 on the top axis shows the range from $\sim$ 15 to $\sim -40$ magnitude, and as discussed in the previous paragraph the system stays in photon-noise limited regime corresponding to a range of object magnitude.

### 4.4 Closed-loop performance

Finally, to assess the full system performance, a closed-loop simulation was carried out following the optical train in Fig. 4.1, including the wavefront-sensing arm. The cuboidal MS which exhibits the better coronagraphic performance of the two designed FPMs was used. 10 phase screens with an input RMS of 0.75 rad and PSD exponent of $-4.5$ were used to run a full closed-loop simulation. For each screen, the aberrated wavefront was propagated to the WFS channel at $1.42\,\mu$m, where it was reconstructed using the non-linear solver (with up to 50 iterations per loop step). The estimated phase was then applied as a correction with a loop gain of 0.7. The corrected wavefront at the coronagraphic wavelength of $1.57\,\mu$m was subsequently propagated through the coronagraph (FPM + Lyot stop) to obtain the peak contrast. This procedure was repeated iteratively for 30 steps, forming a full closed-loop sequence for each of the 10 input screens.

Figure 4.11 shows the evolution of the reconstruction error RMS (at $1.42\,\mu$m) and the peak contrast (at $1.57\,\mu$m) over the closed-loop iterations. Starting from an input RMS of $\sim$ 0.75 rad, the reconstructor requires $\sim$ 7–8 closed-loop steps to reach a reconstruction error RMS of $\sim 10^{-7}$ rad at the wavefront-sensing wavelength. With the applied loop gain of 0.7, this corresponds to approximately $\sim 10^{-3}$ rad at the coronagraphic wavelength over the same number of steps, as shown in Fig. 4.11. At this error RMS, the minimum achievable peak contrast of $\sim 10^{-4}$ is already reached. Note that the peak contrast is defined as the ratio of the maximum pixel value in the coronagraphic image to that in the non coronagraphic image. When the standard deviation of the

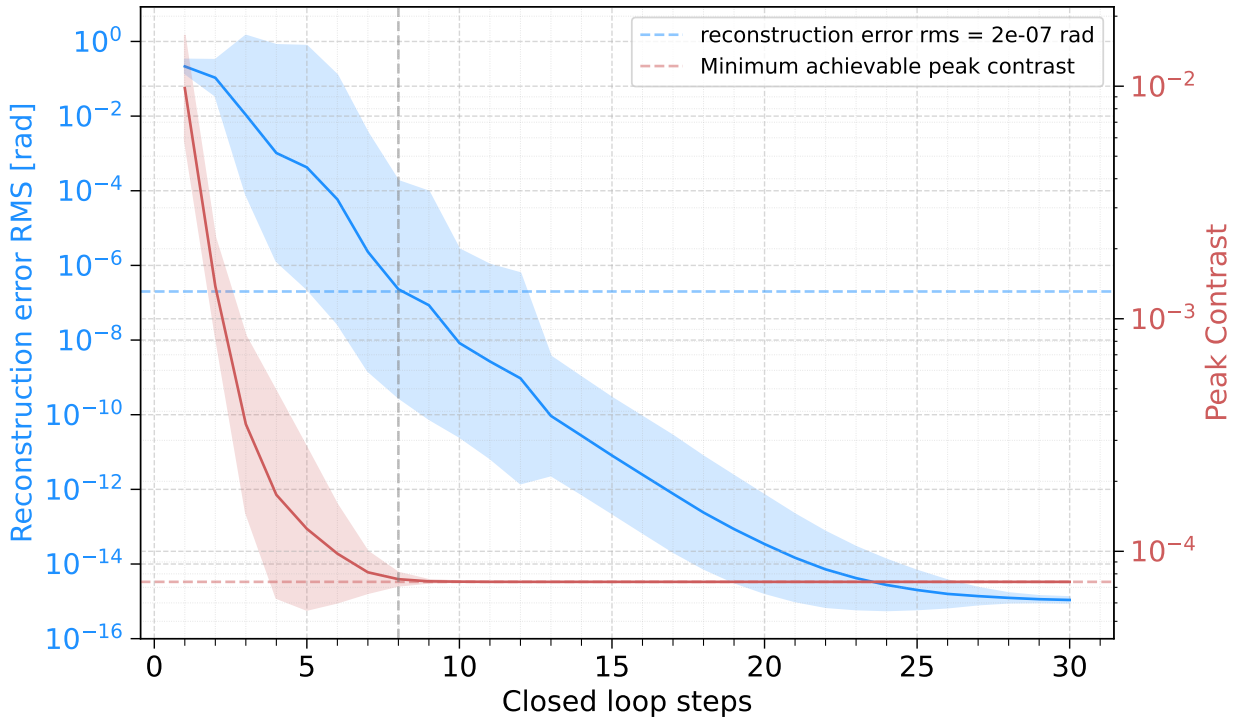


Figure 4.11: Closed-loop performance of the cuboidal MS. The reconstruction error RMS and peak contrast as a function of closed-loop iteration are shown in the red and blue curves, respectively. Results are averaged over 10 phase screens with input RMS and PSD exponent of $-4.5$, where the solid lines indicate the mean and the shaded regions the $1\sigma$ deviations. The vertical gray dashed line marks closed-loop step 8, where the peak contrast saturates at the minimum achievable value of $\sim 2 \times 10^{-4}$. This corresponds to a wavefront reconstruction error RMS of $\sim 10^{-7}$ rad.

peak contrast drops below this limit, it is only an artifact of the metric. The loop still converges toward the true minimum contrast defined by this ratio. Beyond this, further improvement in reconstruction error does not result in improved contrast. Regardless, the reconstructor ultimately reaches machine precision in the wavefront-sensing wavelength after approximately $\sim 30$ closed-loop steps.

It is important to note that this closed-loop simulation assumes an ideal correction in which the phase estimate is directly subtracted from the wavefront. In practice, the correction would be applied using a deformable mirror (DM), meaning the update would be implemented in a DM's modal basis rather than the pixel basis. This would degrade the correction performance and likely raise the floor of the achievable peak contrast.

# Chapter 5

# HOW TO BUILD UP ON THIS WORK?

## 5.1 Summary of the key results

This work demonstrates that a metasurface-based focal-plane mask can serve simultaneously as a CMC and a ZWFS within a PIAA–iPIAA architecture. Specifically, a simple Roddier and Roddier–type mask and a simple ZWFS phase dot were implemented in a single focal-plane optic. Two MS geometries were investigated for this: a cuboidal design and a cylindrical design, with their optical responses summarized in Table 3.1. The cuboidal MS stays within $\lesssim 3\%$ of the ideal phase shifts, whereas the cylindrical MS exhibits slightly larger deviations of $\sim 3\%$ (for cmc) and $\sim 15\%$ (for ZWFS) but achieves higher transmission ($> 95\%$). This allowed for a trade-off study between the effects of phase and transmission on the coronagraphic performance.

Using the complex transmission maps from the FDTD simulations of the MS in the end-to-end MagAO-X model, the optimal mask diameters were found to be $D_{\text{opt}} = 1.41\ \lambda/D$ for the cuboidal MS and $1.36\ \lambda/D$ for the cylindrical MS to obtain the best coronagraphic peak contrast. We also showed that the ideal mask size is largely driven by the complex mask's transmission response. The cuboidal MS reached a peak contrast of $\sim 10^{-4}$ with an inner working angle of $\sim 0.7\ \lambda/D$ and peak throughput of $\sim 70\%$. The coronagraphic PSF closely matched the performance of an ideal $\pi$-phase mask beyond the first Airy ring. The cylindrical MS performed slightly worse, achieving contrasts of order $\sim 10^{-3}$, consistent with its larger phase deviation. Overall, the results show that coronagraphic performance is determined primarily by phase accuracy rather than transmission amplitude, highlighting the importance of precise phase realization in the metasurface design. A scan of different transmission profiles showed that the coronagraphic performance stays the same, but the ideal mask size changes.

On the wavefront-sensing side, both metasurfaces produced very similar responses due to very high transmission ($\gtrsim 95\%$) and also being limited by the fixed mask diameter dictated by the coronagraphic requirements. As a result, the WFS behaviour obtained here is not fully optimized, and is therefore compared against an ideal ZWFS of the same physical size as the MS. The photon-noise sensitivity reached $\sim 1.05$, relative to $\sim 1.15$ for an ideal $\pi/2$ mask, and improved further when the PIAA apodization was included. Dynamic-range tests using a non-linear reconstructor showed that the metasurface WFS performed comparably to the ideal ZWFS for input RMS values between $10^{-4}$ and 0.3 rad. Beyond 0.3 rad the ideal ZWFS performed better, but only marginally relative to the metasurfaces. The reconstruction under photon noise stayed within the noise-limited

regime, where the reconstruction error RMS was driven by the number of available photons and followed $N_\gamma^{-1/2}$. The phase deviation from the ideal $\pi/2$ for the MS was comparatively large $\sim$

An ideal-condition closed-loop simulation with a gain of 0.7 was performed using the better-performing cuboidal MS. The WFS and coronagraphic channel were combined to use the wavefront sensor's phase estimation to correct for the wavefront at the coronagraphic wavelength. The closed loop reached the achievable coronagraphic floor of $\sim 2 \times 10^{-4}$ after $\sim$ 10 loop steps with a non-linear reconstructor capped at 50 iterations. These results demonstrate that a metasurface designed with an appropriate dual-wavelength phase response can effectively support both high-contrast coronagraphy and wavefront sensing in a single focal-plane element.

### 5.2 Towards a more informed design

The proof-of-concept proposed in (S. Y. Haffert, Males, and Oliver Guyon, 2023) was demonstrated here. The results of this thesis also provide a framework for designing hybrid metasurface focal-plane masks (FPMs). Using this framework, a more optimal design can be realized. Two different approaches can be taken.

The first approach uses the end-to-end optical simulation to optimize the complex transmission of the mask in both the coronagraphic and wavefront-sensing bands. Mask designs such as rings or hexagonal sections, beyond a simple phase dot, have shown improved performance for both coronagraphy (Belikov et al., 2018) with complex pupil shapes and wavefront sensing (S. Y. Haffert, Males, and Olivier Guyon, 2023) for increased sensitivity (these geometries essentially provide more degrees of freedom). Additionally, relying on both phase and transmission when optimizing performance can slightly relax the design problem. The figure of merit to optimize would be the metrics measured in this work, namely the peak contrast, throughput, and IWA for coronagraphy, and sensitivity and reconstruction-error RMS for wavefront sensing. Such optimizations can be computationally demanding, especially because a finer pupil grid is required to accurately model the effects from the PIAA–iPIAA optics. A differentiable optical model would therefore be ideal, which could be impl emented within HCIPy as in(Emiel H Por, Pueyo, and Rémi Soummer, 2022; Landman et al., 2022), or using already available tools such as DLux (Desdoigts et al., 2024). Another important consideration is robustness to small deviations from the required phase and transmission values. To address this, each high-performing solution should be evaluated under both negatively and positively biased complex-transmission values, and its performance reassessed. This is important because the metasurface response will not match the optimized complex transmission exactly. To realize the metasurface itself, RCWA simulations for the optimal meta-atoms would need to be carried out again, ideally with differentiable capabilities such as those in `meent` (Kim et al., 2024). The limitation of this approach is the absence of full-wave

FDTD simulations in the optimization loop. These simulations reveal artifacts such as edge effects discussed in Section 3.4. Although FDTD can be run after the metasurface is designed to study these effects, the optimization itself is not informed by them, and they would therefore be treated as post-design artifacts.

This is where the second approach becomes relevant. Instead of optimizing an ideal complex transmission and then realizing it, a topology optimization of the FPM using full FDTD simulations can be employed. This incorporates these artifacts directly into the optimization. Topology optimization also naturally accounts for manufacturing deviations such as over- or under-etching, and has been used successfully in other metasurface applications such as metalenses (Lin et al., 2019). However, this approach introduces significant computational challenges, since FDTD simulations are expensive. Some workarounds, such as enforcing symmetries, could reduce the simulation domain and mitigate computational load.

Another important takeaway from this work is the change in the optimal mask size due to deviations in transmission. To account for transmission mismatch between the designed and manufactured masks, fabricating masks with slightly different sizes could be beneficial.

### 5.3 Outlook

This thesis explored a first demonstration of combining coronagraphy and wavefront sensing in a single metasurface focal-plane mask, motivated by the need for higher-performing coronagraphs and mitigation of NCPAs in high-contrast imaging systems. The results show that the chromaticity of metasurfaces can provide the required different complex transmission responses and support both functions within the same PIAA–iPIAA architecture. While the design approaches outlined in the previous section point toward more optimized masks, the near-term work whould be to manufacture the designed metasurface and carry out the necessary laboratory validation.

**AI Statement:** Artificial intelligence tools were used to improve grammar, clarity, and formatting in parts of this thesis. All scientific content, analysis, and interpretation were performed by the author.

# BIBLIOGRAPHY


Belikov, Ruslan et al. (2018). "Design and performance analysis of a PIAACMC coronagraph on a segmented aperture". In: *Space Telescopes and Instrumentation 2018: Optical, Infrared, and Millimeter Wave*. Vol. 10698. SPIE, pp. 455–464.

Berenger, Jean-Pierre (1994). "A perfectly matched layer for the absorption of electromagnetic waves". In: *Journal of computational physics* 114.2, pp. 185–200.

Bloemhof, Eric E and J Kent Wallace (2003). "Phase contrast techniques for wavefront sensing and calibration in adaptive optics". In: *Astronomical Adaptive Optics Systems and Applications*. Vol. 5169. SPIE, pp. 309–320.

Chambouleyron, Vincent, Olivier Fauvarque, Cédric Plantet, et al. (2022). "Optimizing Fourier-filtering WFS to reach sensitivity close to the fundamental limit". In: *Adaptive Optics Systems VIII*. Vol. 12185. SPIE, pp. 932–944.

Chambouleyron, Vincent, Olivier Fauvarque, Jean-François Sauvage, et al. (2021). "Variation on a Zernike wavefront sensor theme: Optimal use of photons". In: *Astronomy & Astrophysics* 650, p. L8.

Desdoigts, Louis et al. (2024). "Differentiable Optics with dLux II: Optical Design Maximising Fisher Information". In: *arXiv preprint arXiv:2406.08704*.

Foster, Warren (2023). "Implementation of Phase Induced Apodization Optics on MagAO-X". The University of Arizona.

Fusco, Thierry et al. (2016). "SAXO, the SPHERE extreme AO system: on-sky final performance and future improvements". In: *Adaptive Optics Systems V*. Vol. 9909. SPIE, pp. 273–290.

Guyon, Olivier (2003). "Phase-induced amplitude apodization of telescope pupils for extrasolar terrestrial planet imaging". In: *Astronomy & Astrophysics* 404.1, pp. 379–387.

– (2005). "Limits of adaptive optics for high-contrast imaging". In: *The Astrophysical Journal* 629.1, p. 592.

– (2018). "Extreme adaptive optics". In: *Annual Review of Astronomy and Astrophysics* 56.1, pp. 315–355.

Guyon, Olivier et al. (2010). "High performance PIAA coronagraphy with complex amplitude focal plane masks". In: *The Astrophysical Journal Supplement Series* 190.2, p. 220.

Haffert, Sebastiaan Y (2024). "Into nonlinearity and beyond for Zernike-like wavefront sensors". In: *Astronomy & Astrophysics* 683, A113.

Haffert, Sebastiaan Y, Jared R Males, and Oliver Guyon (2023). "Integrated coronagraphy and wavefront sensing with the PIAACMC". In: *Techniques and Instrumentation for Detection of Exoplanets XI*. Vol. 12680. SPIE, pp. 848–854.

Haffert, Sebastiaan Y, Jared R Males, and Olivier Guyon (2023). "Reaching the fundamental sensitivity limit of wavefront sensing on arbitrary apertures with the phase induced amplitude apodized Zernike wavefront sensor (PIAA-ZWFS)". In: *arXiv preprint arXiv:2310.10889*.

Jovanovic, N et al. (2015). "The Subaru coronagraphic extreme adaptive optics system: enabling high-contrast imaging on solar-system scales". In: *Publications of the Astronomical Society of the Pacific* 127.955, p. 890.

Jurling, Alden S and James R Fienup (2014). "Applications of algorithmic differentiation to phase retrieval algorithms". In: *Journal of the Optical Society of America A* 31.7, pp. 1348–1359.

Kenworthy, Matthew A and Sebastiaan Y Haffert (2025). "High-Contrast Coronagraphy". In: *Annual Review of Astronomy and Astrophysics* 63.

Kim, Yongha et al. (2024). "Meent: Differentiable Electromagnetic Simulator for Machine Learning". In: *arXiv preprint arXiv:2406.12904*.

Lagrange, Anne-Marie (2014). "Direct imaging of exoplanets". In: *Philosophical Transactions of the Royal Society A: Mathematical, Physical and Engineering Sciences* 372.2014, p. 20130090.

Landman, Rico et al. (2022). "Joint optimization of wavefront sensing and reconstruction with automatic differentiation". In: *Adaptive Optics Systems VIII*. Vol. 12185. SPIE, pp. 2582–2593.

Lin, Zin et al. (2019). "Topology optimization of freeform large-area metasurfaces". In: *Optics express* 27.11, pp. 15765–15775.

Lyot, Bernard (1939). "The study of the solar corona and prominences without eclipses (George Darwin Lecture, 1939)". In: *Monthly Notices of the Royal Astronomical Society, Vol. 99, p. 580* 99, p. 580.

Macintosh, Bruce et al. (2014). "First light of the gemini planet imager". In: *proceedings of the National Academy of Sciences* 111.35, pp. 12661–12666.

Madhusudhan, Nikku et al. (2014). "Exoplanetary atmospheres". In: *arXiv preprint arXiv:1402.1169*.

Males, Jared R, Laird M Close, Sebastiaan Y Haffert, et al. (2024). "MagAO-X: commissioning results and status of ongoing upgrades". In: *Adaptive Optics Systems IX*. Vol. 13097. SPIE, pp. 47–56.

Males, Jared R, Laird M Close, Kelsey Miller, et al. (2018). "MagAO-X: project status and first laboratory results". In: *Adaptive Optics Systems VI*. Vol. 10703. SPIE, pp. 76–89.

Mayor, Michel and Didier Queloz (1995). "A Jupiter-mass companion to a solar-type star". In: *nature* 378.6555, pp. 355–359.

Moharam, MG and Thomas K Gaylord (1981). "Rigorous coupled-wave analysis of planar-grating diffraction". In: *Journal of the Optical Society of America* 71.7, pp. 811–818.

N'Diaye, M et al. (2016). "Calibration of quasi-static aberrations in exoplanet direct-imaging instruments with a zernike phase-mask sensor-ii. concept validation with zelda on vlt/sphere". In: *Astronomy & Astrophysics* 592, A79.

N'Diaye, Mamadou et al. (2013). "Calibration of quasi-static aberrations in exoplanet direct-imaging instruments with a Zernike phase-mask sensor". In: *Astronomy & Astrophysics* 555, A94.

National Academies of Sciences, Engineering, Medicine, et al. (2021). *Pathways to Discovery in Astronomy and Astrophysics for the 2020s*.

Nobel, Jacob de et al. (2021). "Tuning as a Means of Assessing the Benefits of New Ideas in Interplay with Existing Algorithmic Modules". In: *Proceedings of the Genetic and Evolutionary Computation Conference Companion*. GECCO '21. Lille, France: Association for Computing Machinery, pp. 1375–1384. ISBN: 9781450383516. DOI: 10.1145/3449726.3463167. URL: https://doi.org/10.1145/3449726.3463167.

Palatnick, Skyler et al. (2024). "Achromatizing photolithographically patterned metasurfaces with arbitrary, variable unit cell size". In: *Optics Express* 32.26, pp. 47057–47075.

Patel, Dhwanil and Sebastiaan Haffert (2025). *PIAACMC-ZWFS*. https://github.com/dhwanilpate1/PIAACMC-ZWFS.

Paterson, C (2008). "Towards practical wavefront sensing at the fundamental information limit". In: *Journal of Physics: Conference Series*. Vol. 139. 1. IOP Publishing, p. 012021.

Por, E. H. et al. (2018). "High Contrast Imaging for Python (HCIPy): an open-source adaptive optics and coronagraph simulator". In: *Adaptive Optics Systems VI*. Vol. 10703. Proc. SPIE. DOI: 10.1117/12.2314407. URL: https://doi.org/10.1117/12.2314407.

Por, Emiel H, Laurent Pueyo, and Rémi Soummer (2022). "Joint optimization of multiple optical planes in a stellar coronagraph". In: *Space Telescopes and Instrumentation 2022: Optical, Infrared, and Millimeter Wave*. Vol. 12180. SPIE, pp. 2034–2046.

Roddier, François and Claude Roddier (1997). "Stellar coronograph with phase mask". In: *Publications of the Astronomical Society of the Pacific* 109.737, p. 815.

Rytov, S (1956). "Electromagnetic properties of a finely stratified medium". In: *Soviet Physics JEPT* 2, pp. 466–475.

Seager, Sara and Drake Deming (2010). "Exoplanet atmospheres". In: *Annual Review of Astronomy and Astrophysics* 48.1, pp. 631–672.

Soummer, Remi, Carole Aimé, and PE Falloon (2003). "Stellar coronagraphy with prolate apodized circular apertures". In: *Astronomy & Astrophysics* 397.3, pp. 1161–1172.

Wolszczan, Aleksander and Dail A Frail (1992). "A planetary system around the millisecond pulsar PSR1257+ 12". In: *Nature* 355.6356, pp. 145–147.

Yee, Kane (1966). "Numerical solution of initial boundary value problems involving Maxwell's equations in isotropic media". In: *IEEE Transactions on antennas and propagation* 14.3, pp. 302–307.

Yu, Nanfang and Federico Capasso (2014). "Flat optics with designer metasurfaces". In: *Nature materials* 13.2, pp. 139–150.

Zernike, F (1935). "Phase contrast". In: *Z Tech Physik* 16.454, p. 1.

Zernike, Frits (1934). “Diffraction theory of the knife-edge test and its improved form, the phase-contrast method”. In: *Monthly Notices of the Royal Astronomical Society, Vol. 94, p. 377-384* 94, pp. 377–384.

Zundel, Lauren and Alejandro Manjavacas (2018). “Finite-size effects on periodic arrays of nanostructures”. In: *Journal of Physics: Photonics* 1.1, p. 015004.